PERGAMON

International Journal of Solids and Structures 38 (2001) 8407–8440

INTERNATIONAL JOURNAL OF
SOLIDS and
STRUCTURES

www.elsevier.com/locate/ijsolstr

On transition of delamination growth behaviour for compression loaded composite panels

K.-F. Nilsson *, L.E. Asp [1], A. Sjögren [1]

The Aeronautical Research Institute of Sweden, P.O. Box 110 21, SE-161 11 Bromma, Sweden

Received 9 May 2000; in revised form 7 May 2001

Abstract

This paper presents a combined numerical and experimental study of slender composite panels loaded in compression with artificial delaminations at two different depths. The study was motivated by finite element analyses where this change in delamination depth induced a transition in the direction of delamination growth along with a change in the basic fracture modes and stability. Tests were then carried out to verify the transition in delamination growth. The predicted transitions were to a large extent also seen in the tests. The paper gives an outline of the computational model, which includes contact between delaminated members, calculation of energy release rate with fracture mode separation by an approximate as well as a reliable method for general layups, and moving mesh scheme to account for delamination growth. The experimental work includes monitoring of delamination growth by *C*-scan and acoustic emission along with a detailed fractographical study. The correlation between experimental observations and computed results are discussed in detail. © 2001 Elsevier Science Ltd. All rights reserved.

Keywords: Composite panels; Transition; Growth behaviour

---

1. Introduction

Aerospace composite structures should be designed to resist growth of impact damage that may arise during service. In order to optimize designs, tools that can predict and simulate the effect of typical impact damage become very important. Such tools should be as accurate as possible, yet conservative, and they should be able to handle real and complex aircraft structures. This is a challenging and daunting problem. The complexity arises for a number of reasons. One is that the damage itself tends to be very complex with several, and often interacting, damage types such as delaminations, matrix cracks, broken fibres etc. The material, even when it is undamaged, is anisotropic as well as heterogeneous and the structure could undergo buckling, which necessitates kinematically nonlinear analysis. For a number of years a broad project with the objective to develop such a tool has been ongoing at the Aeronautical Research Institute of

---

* Corresponding author. Present address: Institute for Advanced Materials, Nuclear Safety Unit, European Commission, P.O. Box 2, 1755 ZG Petten, Netherlands. Tel.: +31-224-55-656; fax: +31-224-561-568.

E-mail address: nilsson@jrc.nl (K.-F. Nilsson).

[1] Present address: Swedish Institute of Composites (SICOMP), P.O. Box 104, 431 22 Mölndal, Sweden.

PII: S0020-7683(01)00114-7

Sweden, FFA (e.g. Nilsson et al., 1993, 2001; Asp et al., 1999). In this project, experimental and numerical/theoretical work have been interweaved and the complexity of the analysed problem has been gradually increased.

In recent experiments by Asp et al. (1999), composite panels were first damaged by lateral impact and subsequently loaded in compression until failure. The dominant failure mechanisms was buckling and growth of primarily one delamination. Our effort has therefore initially concentrated on the delamination problem. In particular a design tool, delamination buckling growth and simulation (DEBUGS), that can simulate growth and buckling for delaminations of quite general shapes has been developed. In a recent combined experimental and analytical study by Nilsson et al. (2001), it was shown that delamination growth in slender panels is often controlled by global panel buckling. In virtually all investigations of laminates with embedded delaminations loaded in uniaxial compression, experimental as well as analytical, delamination growth has primarily taken place in a direction perpendicular to the applied load (e.g. Whitcomb, 1989; Nilsson et al., 2001; Greenhalgh et al., 2000). Now, if this were always the case, then prediction of growth direction would be a rather trivial task. Analyses of laminates with embedded delaminations were carried out with DEBUGS for a number of geometry and material combinations to see if growth could occur in a direction other than orthogonal to the loading. By inserting delaminations at different depths in slender composite panels we found that such a transition did occur in the simulations. A series of tests were subsequently performed to see if this transition also occurred when panels were tested in the laboratory. This paper, which can be viewed as a direct extension of the previous work by Nilsson et al. (2001), describes the combined analytical and experimental work that was performed with this objective in mind.

The paper is organized as follows. A brief description of the theoretical model and its numerical implementation is given first. This is followed by a description of the experimental work, which includes testing as well as fractographical analysis. Finally, the correlation between the tests and analysis is discussed and some suggestions for future work are given.

2. Theoretical and numerical model

The theoretical model and its finite element implementation has been reported in a series of papers and a rather complete description can be found in the recent paper by Nilsson et al. (2001). In order to avoid tedious duplication only a synopsis of the method will be given below.

2.1. Kinematical and constitutive assumptions

The model problem, depicted in Fig. 1, is a multilayered panel with thickness $t + T$ composed of an arbitrary number of laminae. It has a single embedded in-plane delamination with a smooth but otherwise arbitrary front, Γ_D at depth t. We assume that the thickness of the delaminated member and the total thickness of the structure are small compared to in-plane dimensions.

We model a damaged panel using two plates in the thickness direction with midsurfaces at $x_3 = t/2$ and $x_3 = -T/2$, respectively. The displacement of the upper and lower plates are governed by the Reissner–Mindlin assumption,

$$\left.\begin{aligned} u_\alpha(x_1,x_2,z) &= \bar{u}_\alpha(x_1,x_2) + z\theta_\alpha(x_1,x_2), \\ u_3(x_1,x_2,z) &= \bar{u}_3(x_1,x_2). \end{aligned}\right\} \tag{1}$$

The subscripts 1 and 2 refer to in-plane quantities, 3 is the direction normal to the mid-surface, and z is the distance from the mid-surface. Greek indices take values from 1 to 2 and θ_α denotes the rotation of a transverse material fibre. An overbar refers to the mid-plane value of the quantity.

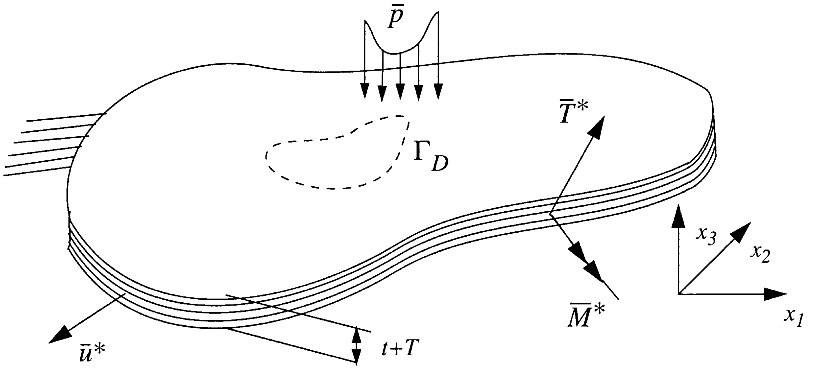

Fig. 1. Multilayered composite plate with a plane crack parallel to an interface.

Small strains and moderate rotations are assumed. The strain tensor may then be written as,

$$\left.\begin{aligned} e_{\alpha\beta} &= e^0_{\alpha\beta} + z\kappa_{\alpha\beta}, \\ e_{3\alpha} &= \tfrac{1}{2}(\bar{u}_{3,\alpha} + \theta_\alpha), \end{aligned}\right\} \tag{2}$$

where $e^0_{\alpha\beta} = \frac{1}{2}(\bar{u}_{\alpha,\beta} + \bar{u}_{\beta,\alpha} + \bar{u}_{3,\alpha}\bar{u}_{3,\beta})$ is the membrane strain and $\kappa_{\alpha\beta} = \frac{1}{2}(\theta_{\alpha,\beta} + \theta_{\beta,\alpha})$ the curvature. The generalized forces conjugate to these quantities can be defined for elastic plates by,

$$N_{\alpha\beta} = \frac{\partial W}{\partial e^0_{\alpha\beta}}, \quad M_{\alpha\beta} = \frac{\partial W}{\partial \kappa_{\alpha\beta}}, \quad 2Q_\alpha = \frac{\partial W}{\partial e_{3\alpha}}, \tag{3}$$

where $W(e^0_{\alpha\beta}, \kappa_{\alpha\beta}, e_{3\alpha})$ denotes the strain energy function.

In the undelaminated domain, displacement continuity is prescribed along the ‘interface’ as illustrated in Fig. 2a, which results in three constraint equations linking the upper and lower plate displacements and rotations,

$$\left.\begin{aligned} \bar{u}^{(U)}_\alpha - \tfrac{t}{2}\theta^{(U)}_\alpha &= \bar{u}^{(L)}_\alpha + \tfrac{T}{2}\theta^{(L)}_\alpha, \\ \bar{u}^{(U)}_3 &= \bar{u}^{(L)}_3. \end{aligned}\right\} \tag{4}$$

Here U and L denote ‘upper’ and ‘lower’. Due to the constraint equations, one may consider the stacked plates as a “two-layer plate model” with seven degrees of freedom for each node in the x_1x_2-plane.

In the delaminated domain, delaminated members are free to separate from each other but are not allowed to penetrate into each other. This leads to a unilateral contact condition that we model by joining nodes with the same in-plane coordinates in the upper and lower delaminated members with linear contact springs. The spring stiffness, K_i, is taken as $2A_iE_{33}/(t+T)$, where A_i denotes the area coupled to the node (the sum of all A_i equals the delaminated area). These ‘contact’ springs have a ‘death–birth option’, which makes it possible to assign zero spring stiffness outside the contact zone and to activate and de-activate contact nodes as the contact area changes. The contact zone and contact forces are computed by a predictor correction method where springs in tension become inactive and springs at node pairs where interpenetration occur become active. The contact analysis has converged when the two convergence conditions,

$$1 - \frac{\sum_{i=1}^{N-N_\mathrm{c}}(d_i)}{\sum_{i=1}^{N-N_\mathrm{c}}(|d_i|)} \leqslant \varepsilon_d, \quad 1 - \frac{\sum_{i=1}^{N_\mathrm{c}}(R_i)}{\sum_{i=1}^{N_\mathrm{c}}(|R_i|)} \leqslant \varepsilon_R, \tag{5}$$

are fulfilled. N is the number of nodes in the delaminated region and N_c the number of nodes with active contact springs, and ε_d and ε_R the two convergence norms. N_c must be determined as part of the nonlinear

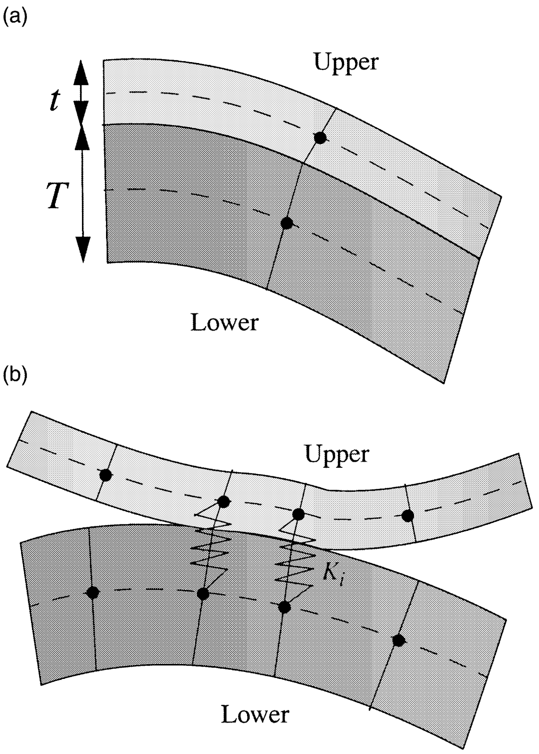

Fig. 2. One-dimensional illustrations of the structural model for (a) undelaminated domain and (b) delaminated domain with active contact springs.

solution. Both criteria are used when contact is partial. When there is full contact, only the force criterion is used, whereas when there is no contact only the displacement criterion is used. In these two special cases the criteria are satisfied exactly. In the present investigation $\varepsilon_d = 10^{-3}$ and $\varepsilon_R = 10^{-2}$ were used.

2.2. Computation of energy release rate and fracture mode decomposition

Delamination growth is assumed to take place when the energy release rate attains a critical value. For interface crack propagation the critical energy release rate depends on the basic fracture modes at the crack tip. This is often expressed as, $G = G_c(\Psi)$ where Ψ is the phase angle defined by $\Psi = a\tan(K_{II}/K_I)$ and where K_I and K_{II} are the stress intensity factors in Mode I and Mode II, respectively (see for instance Hutchinson and Suo (1992)). Mode mixity formulas usually neglect the Mode III effect. For embedded delaminations this is not a serious problem since the Mode III component is usually very small.

The energy release rate at local crack growth, G, can in the present plate theory be computed from the discontinuity in field variables across the crack front of a tensor component, P_{nn},

$$G = (P_{nn}^{(1)} - P_{nn}^{(2)}) + (P_{nn}^{(3)} - P_{nn}^{(4)}). \tag{6}$$

The superscript denotes the location where the tensor, P_{nn}, is evaluated (see Fig. 3b) where

$$P_{nn} = W - N_{n\gamma}\bar{u}_{\gamma,n} - Q_n\bar{u}_{3,n} - M_{n\gamma}\theta_{\gamma,n}, \tag{7}$$

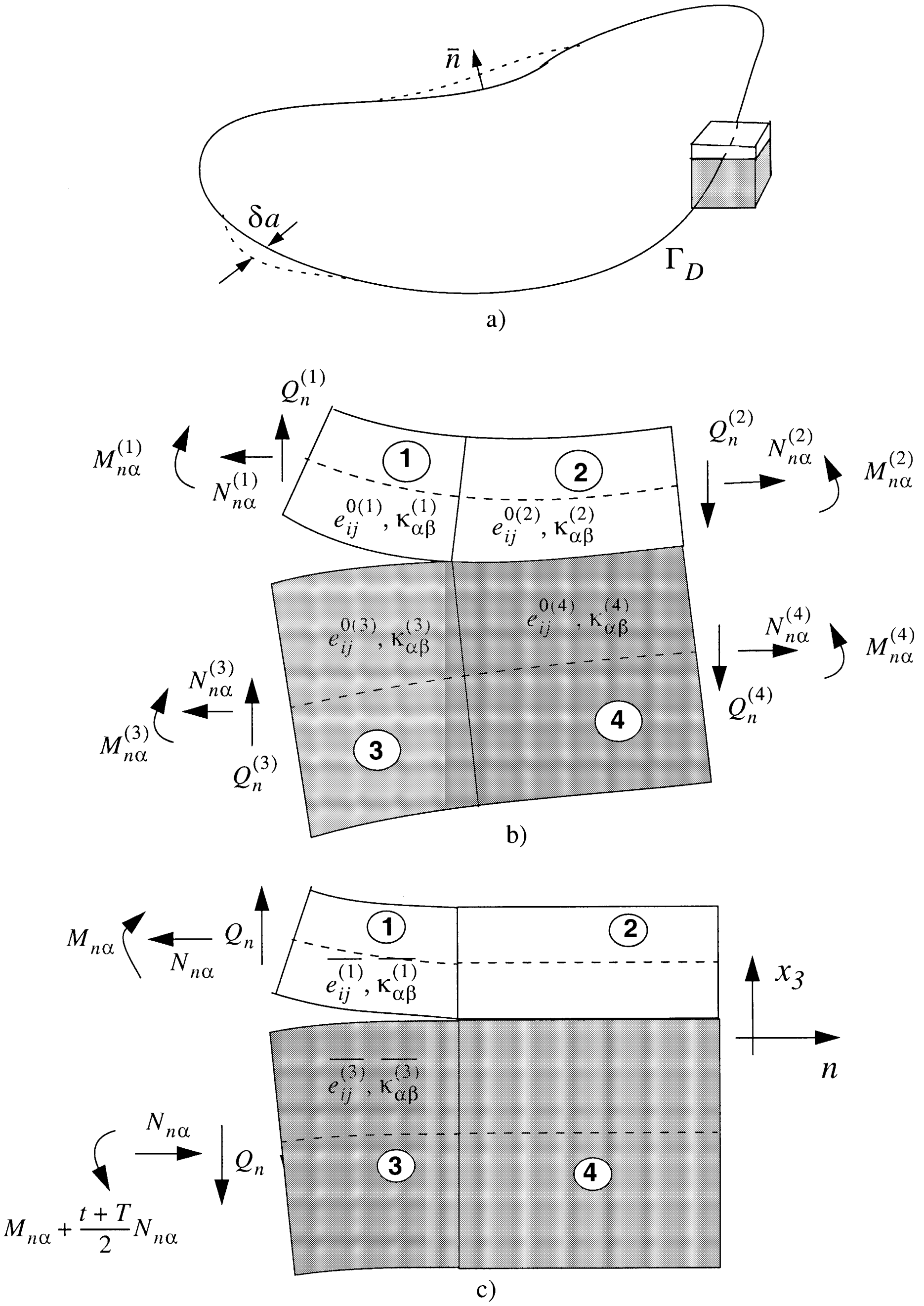

Fig. 3. (a) Smooth delamination growth by an amount δa in local normal direction. Split element with resulting beam sectional forces, (b) prior to superposition and (c) after superposition.

and n denotes the normal direction to the crack front (see Fig. 3a). In Eqs. (6) and (7) summation is done for double Greek indices but not when n appears as double indices.

The nonlinear plate problem can be approximated locally by a linear beam problem by superposing a homogeneous strain field such that the undelaminated region becomes undeformed as illustrated in Fig. 3c, i.e.,

$$\left.\begin{array}{l} \left.\begin{array}{l} \overline{e_{ij}^{0(h)}} = e_{ij}^{0(h)} - e_{ij}^{0(h+1)}, \\ \overline{\theta_{\alpha,\beta}^{(h)}} = \theta_{\alpha,\beta}^{(h)} - \theta_{\alpha,\beta}^{(h+1)}, \end{array}\right\} \quad h = 1 \text{ and } 3, \\ \overline{\theta_{\alpha,\beta}^{(h)}} = \overline{e_{ij}^{(h)}} \equiv 0, \quad h = 2 \text{ and } 4, \end{array}\right\} \tag{8}$$

where superscript h denotes the plate section numbering shown in Fig. 3. Eq. (7) can then be written as

$$\overline{P_{nn}^{(h)}} = \frac{\overline{N_{nn}^{(h)}}\,\overline{e_{nn}^{0(h)}} + \overline{N_{nt}^{(h)}}\,\overline{e_{nt}^{0(h)}}}{2} + \frac{\overline{M_{nn}^{(h)}}\,\overline{\kappa_{nn}^{(h)}}}{2} + \frac{\overline{Q_{n}^{(h)}}\,\overline{e_{3n}^{(h)}}}{2}, \tag{9}$$

where the barred generalized forces denotes that they are conjugate to the deformation field after superposition. The load resultants in the upper and lower part with the sign convention in Fig. 3b are directly related to each other by: $\overline{N_{n\alpha}^{(1)}} = -\overline{N_{n\alpha}^{(3)}} = N_{n\alpha}$, $\overline{M_{n\alpha}^{(1)}} = M_{n\alpha}$, $\overline{M_{n\alpha}^{(3)}} = -M_{n\alpha} - (t+T)/2N_{n\alpha}$ and $\overline{Q_n^{(1)}} = -\overline{Q_n^{(3)}} = Q_n$. The number of unknown load resultants for the split beam is therefore reduced to five ($N_{n\alpha}$, $M_{n\alpha}$ and Q_n). It follows directly from Eq. (8) that $\overline{P_{nn}^{(h)}}^{\circ}$ must be zero for $h = 2$ and 4. The superposition principle was suggested previously by Whitcomb (1986) as well as by Suo and Hutchinson (1990). In their analyses the undelaminated section was modelled as one plate and there was no contribution from the transverse shear forces to the energy release rate since Kirchhoff assumptions were adopted. By virtue of linearity, the stress intensity factors must be linearly functions of the sectional forces, which we may formally write as,

$$\left.\begin{array}{l} K_{\mathrm{I}} = a_1 N_{nn} + a_2 M_{nn} + a_3 Q_n + a_4 N_{nt} + a_5 M_{nt}, \\ K_{\mathrm{II}} = b_1 N_{nn} + b_2 M_{nn} + b_3 Q_n + b_4 N_{nt}^{1^\circ} + b_5 M_{nt}, \\ K_{\mathrm{III}} = c_1 N_{nn} + c_2 M_{nn} + c_3 Q_n + c_4 N_{nt} + c_5 M_{nt}. \end{array}\right\} \tag{10}$$

The coefficients in Eq. (10) may be determined by solving the split beam problem with sectional forces applied one by one.

2.2.1. Approximate mode decomposition

Mode separation for isotropic materials was treated by Nilsson and Storåkers (1992) using closed form results for the split beam problem given by Hutchinson and Suo (1992) and neglecting the transverse shear contribution. The only nonvanishing coefficients are then:

$$\left.\begin{array}{ll} a_1 = \frac{\cos(\omega)}{\sqrt{2tU}}, & a_2 = \frac{\sin(\omega+\gamma)}{\sqrt{2t^3V}}, \\ b_1 = \frac{\sin(\omega)}{\sqrt{2tU}}, & b_2 = \frac{\cos(\omega+\gamma)}{\sqrt{2t^3V}}, \\ & c_4 = \sqrt{\frac{t+T}{2tT}}. \end{array}\right\} \tag{11a}$$

where $\eta = t/(T+t)$ is the thickness ratio, and γ, ω, V and U are geometry functions given by,

$$\left.\begin{array}{ll} 1/V = 12(1+3\eta^3), & 1/U = 1 + 4\eta + 6\eta^2 + 3\eta^3, \\ \gamma = \mathrm{a}\ \sin(\sqrt{UV}6\eta^2(1+\eta)), & \omega = 0.9093 - 0.0524\eta. \end{array}\right\} \tag{11b}$$

Corresponding coefficients for orthotropic materials when principal material axes are normal to the crack front have been given by Suo and Hutchinson (1990), Hutchinson and Suo (1992) and by Shienman and Kardomateas (1997).

This 'isotropic' mode decomposition will be used as an 'approximate mode decomposition' in the simulations of delamination growth in this paper. Thus, stress intensity factors related to the in-plane loads

N_{nn} and M_{nn}, will be calculated using Eqs. (10), (11a) and (11b). The contribution from the shear force, Q_n, will be assumed pure Mode I loading. This assumption is based on results from the reliable finite element analysis of the split beam problem outlined below and which will be demonstrated in the results section. Thus, the stress intensity factors may then be written as,

$$\left.\begin{aligned} K_{\mathrm{I}} &= K_{\mathrm{I}}^{\mathrm{iso}} + K_{\mathrm{I}}^{Q}, \\ K_{\mathrm{II}} &= K_{\mathrm{II}}^{\mathrm{iso}}. \end{aligned}\right\} \tag{12}$$

Here the superscript 'iso' denotes that the stress intensity factors have been computed using the coefficients given in Eqs. (11a) and (11b). The shear force stress intensity factor, K_{I}^{Q}, is taken as,

$$K_{\mathrm{I}}^{Q} = \sqrt{E_{nn} G_Q}, \tag{13}$$

where E_{nn} is the Young's modulus of the delaminated member in the direction normal to the front and G_Q the contribution to the energy release rate from the shear forces. A negative K_{I} would indicate that the crack tips overlap locally. Such overlap is not physically feasible and instead we will assume that the loading then will be pure Mode II. Thus, the phase angle will have the form,

$$\left.\begin{aligned} &\Psi = \arctan(K_{\mathrm{I}}/K_{\mathrm{II}}), \quad K_{\mathrm{I}} \geqslant 0, \\ &\Psi = 90^\circ, \quad K_{\mathrm{I}} < 0, \quad K_{\mathrm{II}} > 0, \\ &\Psi = -90^\circ, \quad K_{\mathrm{I}} < 0, \quad K_{\mathrm{II}} < 0. \end{aligned}\right\} \tag{14}$$

2.2.2. Reliable mode decomposition

The crack tip stress field depends on the layup sequence, material properties and loading. In general, fibres are not normal to the crack front and all three fracture modes will therefore be coupled. The split beam problem then has to be solved numerically under generalized plain strain for the particular material combination.

Procedures for reliable calculation of stress intensity factors along crack fronts in piecewise homogeneous and orthotropic materials have been implemented in the FE-solver STRIPE. The procedure is as follows; First an *hp*-version of the finite element method is used to calculate the displacements, u_i. Secondly a so-called advanced extraction procedure is used (Andersson et al., 1990; Andersson, 1993), to extract complex-valued stress intensity functions, $C_{k,m}$, in the expressions,

$$\left.\begin{pmatrix} u_n(x_n,x_t,x_3) \\ u_t(x_n,x_t,x_3) \\ u_3(x_n,x_t,x_3) \end{pmatrix} = \sum_{m=1}^{3}\sum_{k=1}^{6} C_{k,m}(x_t)[Z_k(x_n,x_3)]^{\lambda^{(m)}} \begin{pmatrix} \Phi_1^{(k,m)}(x_n,x_3) \\ \Phi_2^{(k,m)}(x_n,x_3) \\ \Phi_3^{(k,m)}(x_n,x_3) \end{pmatrix}\right\}, \tag{15}$$

which uniquely characterize the displacements near the delamination front. In Eq. (15), $Z_k(x_n,x_3)$ and $\Phi(x_n,x_3)$ are complex functions derived according to the theory of Lekhnitskii (1963) and $\lambda^{(m)} m = 1,2$ and 3, the complex singularity exponents (Wang and Choi, 1982). For the crack problem $\lambda^{(m)} = 0.5$ and $0.5 \pm \mathrm{i}\varepsilon$. In most practical situations the singular term, ε, is very small compared to unity, and exactly zero when the materials on either side of the interface are identical. When, $\varepsilon \neq 0$, singular oscillatory stresses and interpenetration close to the crack tip occur. This region is usually very small. The exception occurs when ε is large and loading is predominantly shear. The problem is discussed in depth by Rice (1988) and Hutchinson and Suo (1992). Since stresses oscillate with increasing frequency as the crack tip is approached, 'classical' stress intensity factors and associated mode ratio and phase angle cannot be defined. This difficulty can be overcome by eliminating the oscillatory behaviour, i.e. prescribe $\varepsilon = 0$. Another, and more consistent approach is to define a length, r_0, and define the phase angle as related by $\Psi = \mathrm{a}\tan[\tau_{n3}(r_0)/\sigma_{33}(r_0)]$. Another measure of the stress intensities is,

$$\left.\begin{aligned} K_1(x_t) &= \lim_{x_n\to 0} \textstyle\sum_{m=1}^{3} \sum_{k=1}^{6} (\sqrt{2\pi}) x_n^{(1-\lambda^{(m)})} \sigma_{33}^{(k,m)}(x_n, x_t, 0), \\ K_2(x_t) &= \lim_{x_n\to 0} \textstyle\sum_{m=1}^{3} \sum_{k=1}^{6} (\sqrt{2\pi}) x_n^{(1-\lambda^{(m)})} \tau_{n3}^{(k,m)}(x_n, x_t, 0), \\ K_3(x_t) &= \lim_{x_n\to 0} \textstyle\sum_{m=1}^{3} \sum_{k=1}^{6} (\sqrt{2\pi}) x_n^{(1-\lambda^{(m)})} \tau_{3t}^{(k,m)}(x_n, x_t, 0), \end{aligned}\right\} \tag{16}$$

where $\sigma_{33}^{(k,m)}$, $\tau_{n3}^{(k,m)}$ and $\tau_{3t}^{(k,m)}$ are calculated from the edge eigenfunctions and the calculated complex stress intensity functions. The first and second summation refer to the three singular eigenfunctions and the six Lekhnitskii functions. The definition for the stress intensity factor in Eq. (16) was introduced by Wang and Choi (1982) and then denoted as 'boundary layer singularities'. These stress intensity factors are uniquely defined real quantities. This is the stress intensity factors we will use for 'reliable mode decomposition' in this paper. Note though that the solution embodied in Eq. (16) contains the complete solution and the two other approaches for determining mode mixity can be adopted as special cases. As long as the interpenetration region is small, and r_0 is chosen outside this region, the three alternatives give very similar phase angle values.

The finite element mesh of the split beam with a delamination at the fourth interface, used for assessment of the approximate mode separation, is depicted in Fig. 4. Each layer is modelled with one element and a refined mesh is used at the crack tip. Rigid body motions are inhibited and the two surfaces $A_1A_2A_3A_4$ and $B_1B_2B_3B_4$ are constrained to have the same displacements. These periodic boundary conditions give generalized plane strain conditions. The polynomial level, p, of each element can be chosen from 2 to 13.

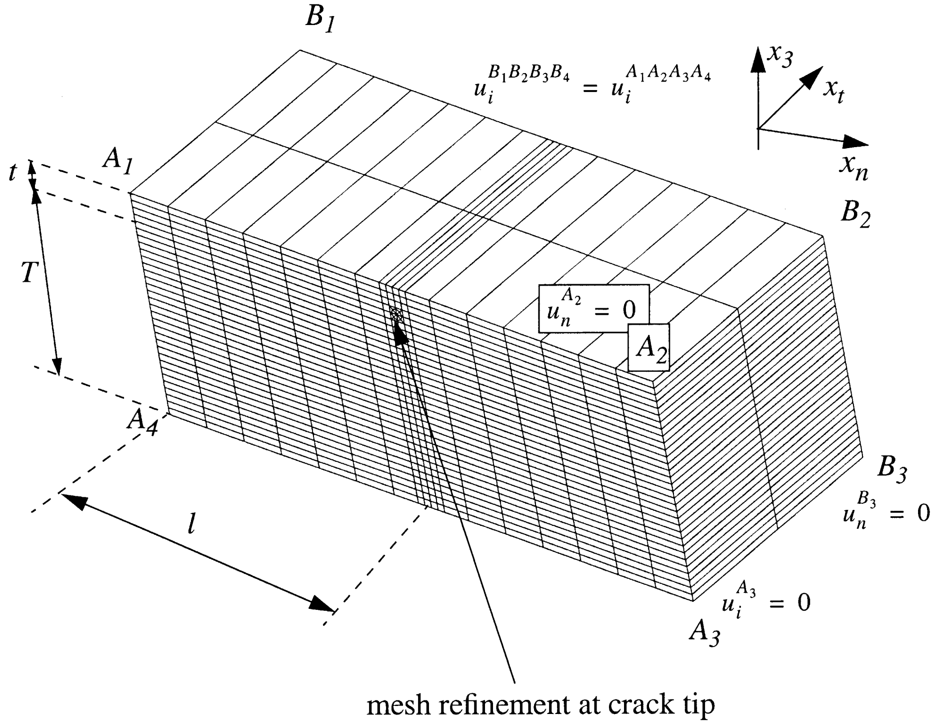

Fig. 4. Finite element mesh of the split beam along with adopted boundary conditions used in the reliable fracture mode decomposition.

2.3. Other damage mechanisms

Other damage mechanisms that interact with the delamination growth may occur. The so-called Hashin criteria (Hashin, 1980), have the advantage over some other stress based criteria since they distinguish between the different failure modes associated with fibre failure and matrix cracking in tension and compression. The criteria are based on the six failure stresses: X_t and X_c tensile and compressive failure stress in fibre direction; Y_t and Y_c tensile and compressive failure stress transverse to fibre direction; S_{FT} in-plane shear failure stress; and S_{t3} transverse shear failure stress. Fibre failure in tension, $\sigma_F > 0$, or compression, $\sigma_F < 0$, will occur when the two respective inequalities (17a) and (17b) are satisfied,

$$\frac{\sigma_F^2}{X_t^2} + \frac{\tau_{FT}^2 + \tau_{F3}^2}{S_{FT}^2} > 1, \tag{17a}$$

$$\frac{\sigma_F}{X_c} > 1. \tag{17b}$$

Likewise, matrix failure in tension, $(\sigma_T + \sigma_3) > 0$, or compression $(\sigma_T + \sigma_3) < 0$, occur when the inequalities (17c) and (17d) are satisfied.

$$\frac{(\sigma_T + \sigma_3)^2}{Y_t^2} + \frac{\tau_{T3}^2 + \sigma_T\sigma_3}{S_{t3}^2} + \frac{\tau_{FT}^2 + \tau_{F3}^2}{S_{FT}^2} > 1, \tag{17c}$$

$$\frac{(\sigma_F + \sigma_3)\left[1 - \left(\frac{Y_c}{2S_{t3}}\right)^2\right]}{Y_c} + \frac{(\sigma_F + \sigma_3)^2}{4S_{t3}^2} + \frac{(\sigma_T^2 - \sigma_T\sigma_3)}{S_{t3}^2} + \frac{(\tau_{FT}^2 + \tau_{F3}^2)}{S_{FT}^2} > 1. \tag{17d}$$

In Eqs. (17a)–(17d), σ_F, σ_T and τ_{FT}, refer to normal stress in the fibre direction, transverse to the fibre direction and in-plane shear stress, respectively, and τ_{F3} and σ_3 refer to transverse shear stress and to peel stress respectively.

2.4. Numerical procedure

The test panels have been analysed with the structural model described above using four-noded (degenerated) isoparametric shell elements implemented in the commercial FE-code ADINA. A plane projection of the adopted FE-mesh with applied boundary and symmetry conditions is shown in Fig. 5. The same mesh has been adopted for the lower and upper part.

The plate parts above and below the delamination are modelled as two separate layered plates. A complete analysis of delamination buckling and growth includes the following steps:

- The global (plate) buckling load is first determined for the structure by imposing the constraints Eq. (4) in the delaminated region and performing the eigenvalue analysis.
- The delamination buckling load is subsequently determined with due account of contact at buckling following the contact procedure outlined above.
- This is followed by the kinematically nonlinear postbuckling analysis where full Newton method is adopted and where the contact analysis is performed at each load. Once the contact analysis has converged, the energy release rate is computed along with fracture mode separation (in the present implementation only the approximate one) and the load is increased automatically.
- The front may propagate when the crack growth criterion, $G(\Psi) = G_c(\Psi)$, has been attained at some node. The front is then advanced by moving the nodes that have reached the crack growth criterion a small distance in the local normal direction to the front and in the plane of the delamination, followed

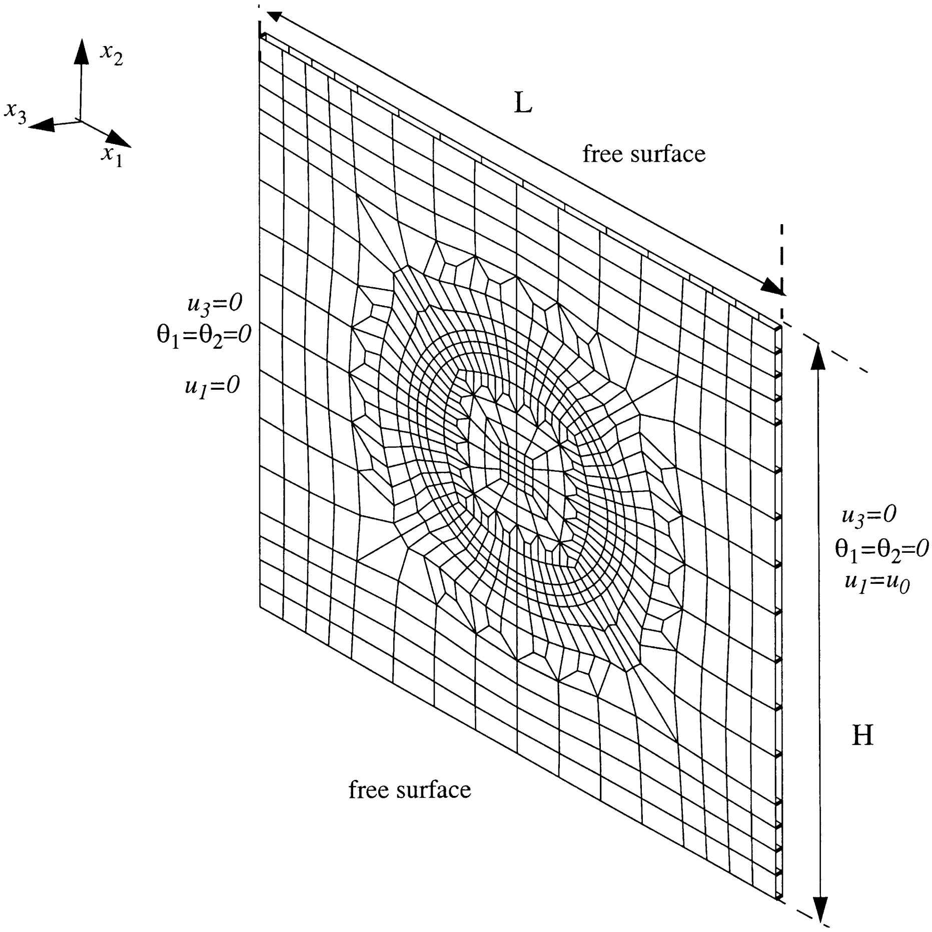

Fig. 5. Finite element mesh used in the analyses at initial growth and applied boundary and symmetry conditions.

by a step where the entire mesh is slightly moved. The postbuckling analysis is then restarted at the previous propagation load, but with the new updated mesh.

3. Experimental methods

3.1. Test specimens

Carbon fibre/epoxy laminates with 32 plies were tested. Three panels were tested without delamination and six panels with implanted artificial delamination. The quasi-isotropic layup $[90/\mp45/0_2/\pm45/90/0/\pm45/90_2/\mp45/0]_2$ was chosen, where the 0°-direction is parallel to the x_1-direction (see Fig. 6). The adopted layup was specially selected to obtain laminates with quasi-isotropic membrane and bending stiffness, but without any bending-stretching or bending-twisting coupling. Symmetrical layups composed of the same plies have identical membrane and membrane-bending properties, but generally show orthotropic bending properties and bending-twisting coupling since plies closer to the mid-plane contribute less to the bending stiffness.

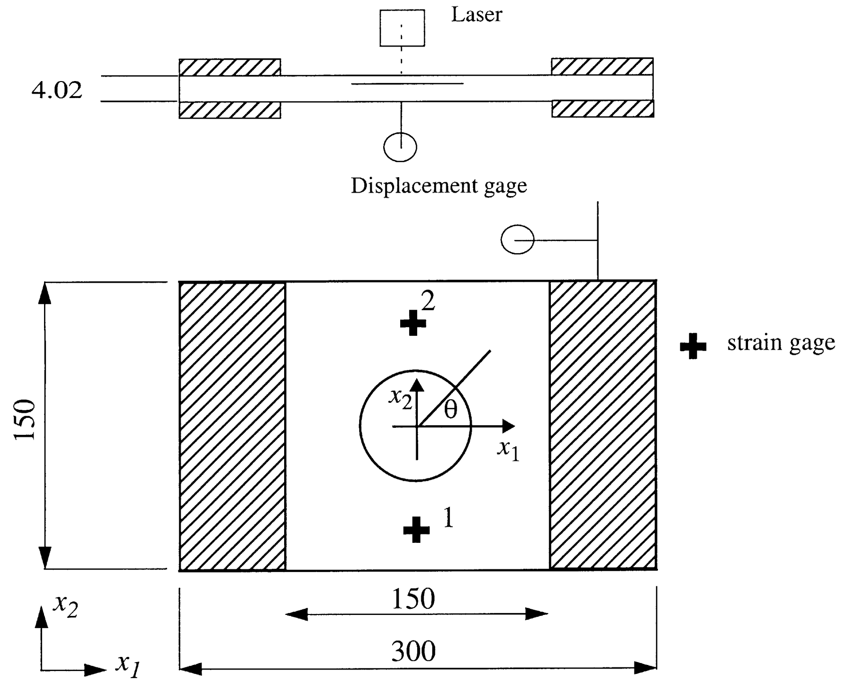

Fig. 6. Schematic top and side view of the delaminated composite plate (lengths in mm).

The artificial delamination was created by a 10 μm thick teflon film with a diameter of 60 mm. The Teflon film was implanted in three plates at the ninth (0/+45) ply-interface and in three plates at the 27th (−45/90) ply-interface (i.e. fifth ply-interface from the bottom). As mentioned in the introduction, the locations of the delaminations were based on preliminary studies that predicted a shift in the direction of delamination growth. Delamination growth for the plates with delamination at the 27th interface was expected to be orthogonal to the applied load direction whereas for the ninth ply-interface, propagation was predicted in the load direction. For brevity, throughout this paper, the 27th ply-interface (fifth from bottom and thickness $t/T = 0.1562$) and ninth ply-interface delaminations ($t/T = 0.2812$) are referred to as the *shallow* and *deep* delaminations respectively. The laminates were manufactured from HTA/6376C prepreg, supplied by Hexcel. The mechanical properties of a unidirectional lamina were: $E_{11} = 131$ GPa (in compression); $E_{22} = E_{33} = 11.7$ GPa; $G_{12} = G_{13} = 5.2$ GPa; $G_{23} = 3.9$ GPa; $\nu_{12} = \nu_{13} = 0.30$; and $\nu_{23} = 0.50$. The nominal ply thickness of each ply was 0.13 mm. The measured thickness of the laminates was 4.16 mm with a standard deviation of 0.04 mm. The panels contain a resin rich layer with very low stiffness at the two surfaces. The height of these resin rich layers has been determined to be 0.07 mm in a previous study (Juntti et al., 1999). Therefore, throughout this study, the load-bearing thickness 4.02 mm will be assumed.

The fracture toughness for uniaxial layups of this material has been determined (Juntti et al., 1999) using delaminated beam tests. The fracture toughness had a strong fracture mode dependence with fracture toughness 250 J/m^2 in pure Mode I and 1000 J/m^2 in pure Mode II. The mixed mode fracture toughness can for most materials be accurately described by a three-parameter relation, $G_C(G_{IC}, a_1, \lambda; \psi)$, where,

$$\left.\begin{aligned} G_C &= G_{IC}[a_1 f_1(\psi,\lambda) + (1-a_1) f_2(\psi,\lambda)], \\ f_1(\psi,\lambda) &= 1 + (\tan([1-\lambda]\psi))^2, \\ f_2(\psi,\lambda) &= \frac{1}{1+(1-\lambda)\sin^2(\psi)}. \end{aligned}\right\} \tag{18}$$

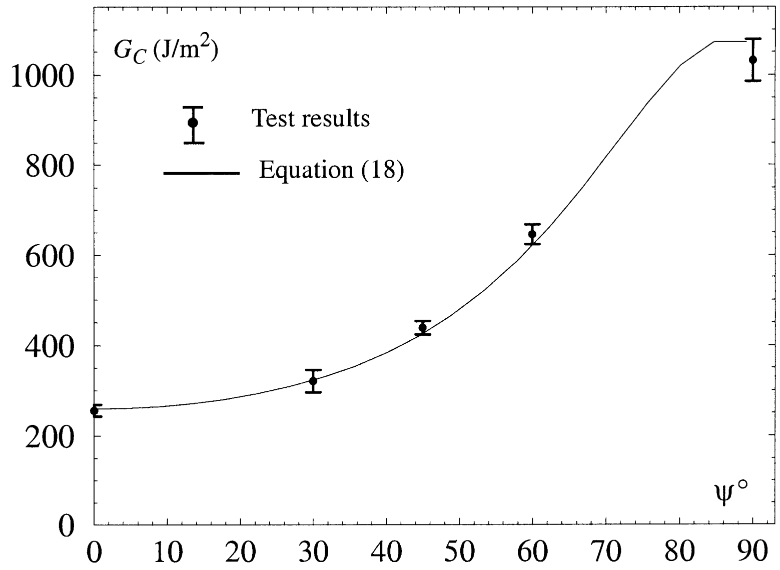

Fig. 7. Critical energy release rate as function of phase angle determined from MMB-test and fitted curve with $G_{IC} = 250$ J/m^2, $\lambda = 0.22$ and $a_1 = -0.10$ in Eq. (18).

The three parameters G_{IC}, a_1 and λ, for a specific material, are determined by fitting Eq. (18) to test results. The measured fracture toughness and the fitted curve with $G_{IC} = 250$ J/m^2, $\lambda = 0.22$ and $a_1 = -0.10$ are shown in Fig. 7.

The Hashin failure criteria (Hashin, 1980) were employed to predict initiation of other failure mechanisms than delamination growth, i.e. matrix cracking and fibre failure. However, no strength data were determined for these particular panels. Instead, typical strength values of the carbon fibre composite were assumed to be: $X_t = 2090$ MPa, $X_c = 1720$ MPa, $Y_t = 112$ MPa, $Y_c = 346$ MPa and $S_{FT} = 131$ MPa (Levin and Jarlås, 1997).

3.2. Test procedure

The test coupons were loaded in an MTS servo-hydraulic testing machine with a maximum load capacity of 250 kN with a manual displacement control. In all tests, the load was applied in the x_1-direction at ambient conditions. As described in Nilsson et al. (2001), the machine clamping force did not produce satisfactory clamped boundary conditions. For this reason, steel plates were bonded on to all coupons by a room temperature curing adhesive. The nominal distance between the clamps (i.e. panel free length) was 150 mm. During the bonding the steel plates could slide slightly, which resulted in a deviation of about 1 mm of the free length. To evaluate uniformity of uniaxial loading, all plates were instrumented with 0°/90° strain gauges. Two strain gauges were bonded on each face of the plates, (see Fig. 6).

In-plane displacement of the steel clamp and out-of-plane displacement in the centre of the substrate (i.e. the thicker member) were measured by dial gauges. In the earlier study, Nilsson et al. (2001), we found that the small point load from the dial gauge spring could delay delamination buckling. To avoid this, out-of-plane displacement of the thinner delaminated member was measured by a noncontact laser instrument.

The plates were scheduled to be tested in the following sequence: In the first load sequence the load at which the delaminated member buckled was determined. In the second load sequence, or in the continuation of the first load sequence, the coupons were loaded until global plate buckling or initial delamination crack growth took place, whichever occurred first. In case of stable delamination growth, the second load sequence was repeated to achieve a number of growth increments. Acoustic emission was used to detect onset of damage growth. To monitor possible delamination crack growth, the plates were dismounted and analysed by ultrasonic *C*-scan after each load sequence. Panel failure may lead to large transitient loads that could damage the functioning of the test machine. Due to this, panels were not intentionally loaded to failure. After testing, the delamination growth regions were cut open, the fracture surfaces gold sputter coated and examined by scanning electron microscopy (SEM) at magnifications between ×50 and ×20 000.

4. Fractographical method

Fractography can be extremely useful for studying failure of polymer-matrix composite components. In particular, it can be used to determine the damage types involved, direction of crack growth and fracture mode loading. The fractographic features associated with interlaminar fracture in carbon fibre/epoxy laminates have been the subject of numerous investigations (e.g. Purslow, 1986; Hahn and Johannesson, 1983; Choi et al., 1999; Singh and Greenhalgh, 1998; Asp et al., 2001). The morphology of the crack surfaces is characterized by the fracture modes. Mode I failure is generally characterized by cleavage, feathering, river lines, scarps, fibre bridging, etc., whereas Mode II failure is characterized by cusps, debris, fibre/matrix debonding, etc. and the Mode III failure by river lines, steps, shear crevices, etc. In a mixed-mode failure a mix of the features characteristic for the Modes I, II and III loading modes can be seen and their relative proportions can then be used to assess the mode mixity.

Interpretation and understanding of the failure mechanisms by fractography is to a large extent based on experience from previous studies of failure. As a basis for the fractographical study in this paper, two sets of typical interlaminar fracture surfaces in carbon fibre/epoxy composites for different Modes I and II ratios are presented in Fig. 8.

The first three micrographs (Fig. 8a–c) stem from in-house beam tests of the material used here and illustrate crack surfaces at static loading with (a) 0% Mode II (pure Mode I), (b) 50% Mode II, and (c) 100%

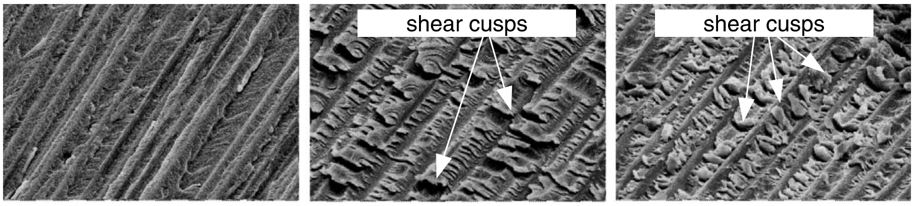

a) 0% Mode II, 0°/5° interface b) 50% Mode II, 0°/5° interface c) 100% Mode II, 0°/5° interface

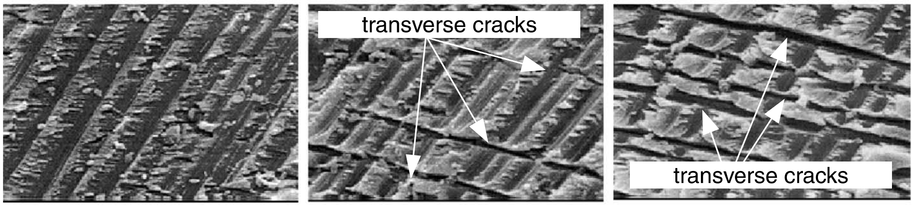

d) 25% Mode II, 0°/90° interface e) 50% Mode II, 0°/90° interface f) 75% Mode II, 0°/90° interface

Fig. 8. Fracture surfaces for two sets of layups and three mode I/II mixity ratios.

Mode II. The layup was uniaxial but with a 5° off-set in one of the layers at the delamination. In the Mode I loading, the crack grew in the resin-rich region between the 0°/5° plies, resulting in a typical cleavage failure. When the Mode II loading increased to 50%, the delamination migrated to the upper fibre boundary, leaving fibre imprints at the lower fracture surface. The formation of cusps seen in the mixed mode loading is the most notable difference with the pure Mode I case. These cusps are relatively thin and flat with a small inclination angle. When the crack was loaded in pure Mode II, growth remained in the upper fibre boundary, but the cusps became thicker, more numerous, and had a higher inclination angle than the cusps formed under 50% Mode II loading. The gradual difference for the observed cusps with increasing Mode II loading is primarily due to a larger angle between small matrix cracks and the delaminated interface which results in larger, deeper and more numerous cusps.

The second set of micrographs (Fig. 8d–f) are taken from Singh and Greenhalgh (1998) and show another typical feature for increasing Mode II loading of MMB-tests. In this case delamination growth was in a 0°/90° interface. In the 25% Mode II case (Fig. 8d) the fractographic features are similar to those seen in pure Mode I conditions of the uniaxial layup. However, as the proportion of Mode II loading increases, transverse cracks, originating from the 90° fibres below the surface can be observed and when the Mode II loading has increased to 75%, a regular grid pattern is produced with one imprint from almost every 0° fibre and one transverse crack from almost every 90° fibre adjacent to the interlaminar layer. When the transverse cracks opened up further at high Mode II content, rudimentary shear cusps can also be seen in the rectangular zones between the grid lines.

Fractography can be used to assess qualitatively the proportion of the fracture modes. In the two sets of micrographs in Fig. 8, increased Mode II loading was manifested by shear cusps or transverse cracks. In the literature it has been suggested that the mode mixity can be determined very accurately from fractography only. However, as seen from Fig. 8, the exact features may differ for different materials and layups and an accurate determination of the mode mixity by fractography requires a complete and detailed characterization of the material system.

5. Results

5.1. Assessment of the approximate fracture mode decomposition

The approximate mode decomposition defined by Eqs. (10)–(14) will be used in the numerical simulations of delamination growth. To assess the error associated with the approximate mode decomposition, we first computed the phase angle with N_{nn}, Q_n and M_{nn} applied as unit loads one-by-one, using the approximate mode decomposition and the full finite element solution with stress intensity factors defined by Eq. (16). In the finite element analyses, each layer was modelled separately and with a mesh refinement at the crack tip. The finite element model and the boundary conditions are depicted in Fig. 4. Membrane forces, N_{nn} were imposed as constant stresses, moments; M_{nn}, as linearly varying stresses and shear forces, Q_n with parabolic distribution. In order to eliminate the length effect in the finite element model for the shear force, a moment pair lQ_n was also imposed. Analyses were done with polynomial orders $p = 2$–5 to ensure that the numerical errors were negligible.

The computed phase angles versus delamination depth are shown in Fig. 9 for the two layups $[90/\mp 45/0_2/\pm 45/90/0/\pm 45/90_2/\mp 45/0]_2$ (Fig. 9a) and $[0/\pm 45/90_2/\mp 45/0/90/\mp 45/0_2/\pm 45/90]_2$ (Fig. 9b) of split beam. The angles in the split beam are defined relative to the normal direction of the crack front. The first layup is identical to the defined panel layup used in the test. The stacking sequence of the second layup is identical to the first layup when counted from the bottom, but it can also be obtained from the first layup by rotating all plies by 90°. Referring to Fig. 9, a split beam problem with the first and second layup

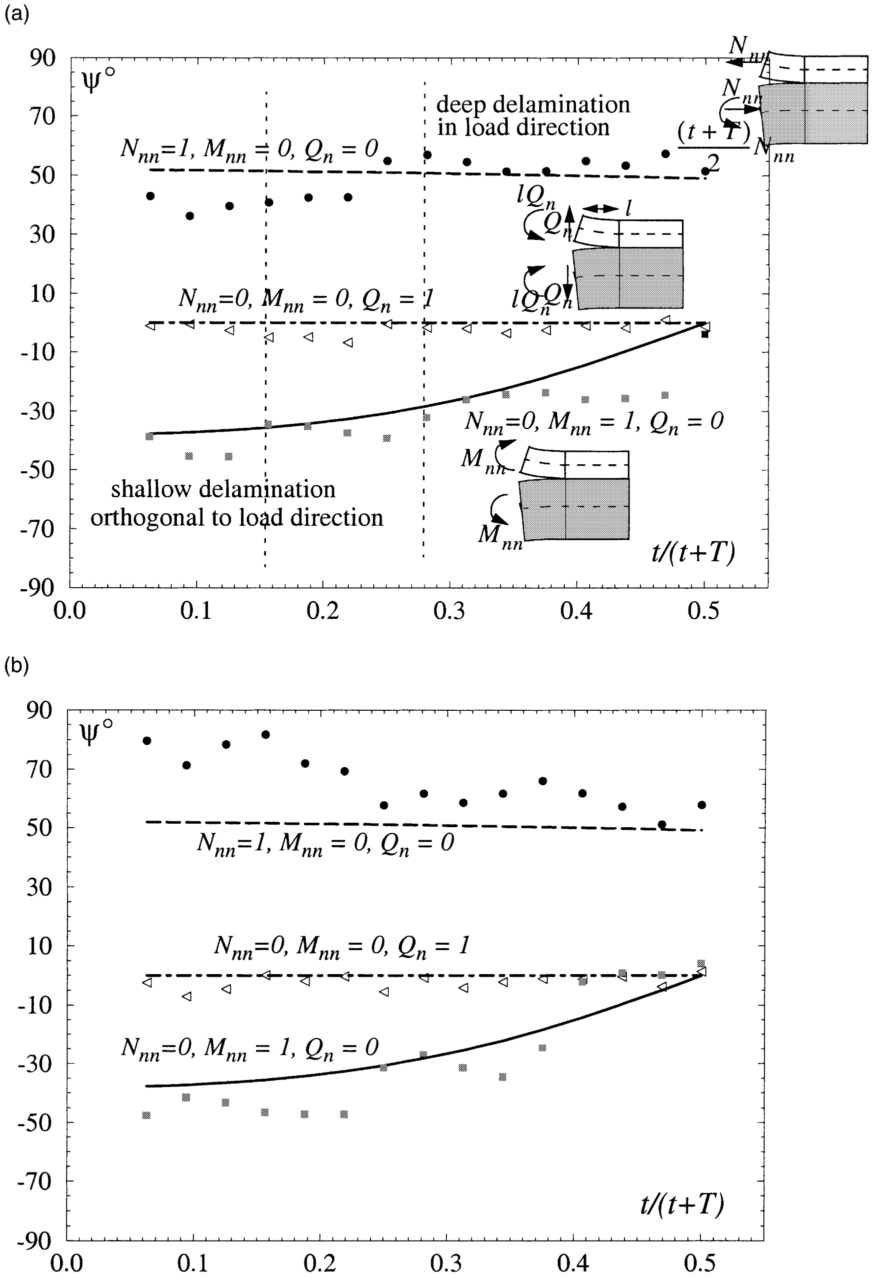

Fig. 9. Computed phase angle, ψ, in degrees for the split-beam as function of delamination depth, $t/(t+T)$, for the three in-plane unit loads. Lines represent the approximate isotropic solutions and symbols the full FE-solutions. (a) $[90/\mp45/0_2/\pm45/90/0/\pm45/90_2/\pm45/0]_2$ and (b) $[0/\pm45/90_2/\mp45/0/90/\mp45/0_2/\pm45/90]_2$.

therefore corresponds to a crack segment with the crack normal in the x_1- and x_2-direction ($\theta = 0°$ and $90°$ in Fig. 6) respectively. If the delamination depth is defined from the bottom the roles of the layups are reversed.

In Fig. 9a and b, lines represent the 'approximate mode decomposition' and the symbols the full finite element solution with delamination located at the second to the sixteenth interface. The two particular cases corresponding to growth in the loading direction for the deep delamination and in the direction orthogonal to the load direction for the shallow delamination are marked with dotted lines. The following observations can be made from Fig. 9: the error in the computed phase angle is slightly larger for the second layup; the pure Mode I assumption for the shear force load case is a very good approximation for both layups and all depths; for the two cases of deep delamination with growth normal to the load direction and shallow delamination with growth orthogonal to the load direction (represented by vertical lines), the error in mode decomposition is relatively small. The Mode III stress intensity factor was generally very small compared to the Mode I and II stress intensity factors. The largest Mode III coupling by far was attained for the split beam with the first layup, delamination at the third interface and bending load. In that case K_{III} attained 25% of the K_{I} and K_{II} values. The imaginary part of the phase angle, which governs the size of oscillatory region, attained its largest value ($\varepsilon = 0.03$ rad), as expected, for 0/90 interfaces.

The error in the mode separation along the entire front of a delamination at a particular interface can be assessed by a sequence of analyses where the stacking sequence in the split-beam problem is incrementally rotated. Fig. 10a shows computed phase angles for the first layup as function of the rotation of the stacking sequence, ϕ, for $\phi = 0°–180°$, and the delamination inserted at the nineth interface. Corresponding results for the second layup and with delamination in the fifth interface are plotted in Fig. 10b. These two plots corresponds to the deep and shallow delamination respectively with ϕ interpreted as the angle of rotation from the loading direction as defined in Fig. 6. We see that for the deep delamination, the error induced by the approximate mode decomposition is relatively small for all three load cases, in particular in the loading direction where initial growth is expected ($\phi = 0°$). The approximate mode decomposition gives a larger error for the shallow delamination, in particular for the membrane load case. However, in the direction orthogonal to the load, and where incipient growth is expected, ($\phi = 90°$) the error is not very large.

5.2. Overall experimental observation

Test results for the panels with shallow and deep delaminations are summarized in Tables 1 and 2. The specimen number provides information on the panel number and load step, i.e. specimen number 1_2 refers to the first panel at the second load sequence. The labels P_{DB} and $P_{\max}$ refer to delamination buckling and maximum loads. The delamination buckling load was taken as the load where onset of a nonlinear relation between the applied load and the out-of-plane deflection of the delaminated member was observed. As we will see below, due to imperfections and to some extent nonsymmetry, this value is not always well defined. P_{growth} and δ_{growth} refer to the load and edge displacement at onset of delamination growth and Δa is the subsequent incremental delamination growth in mm at each load step. For panels with the shallow delamination, Δa was determined as the average growth in the two delamination growth regions. For panels with the deep delamination, however, growth mainly took place on one side and Δa refers to the observed growth of that lobe. The loading was stopped when AE-activity was recorded. From Table 2 we see that for the deep delamination, there was no delamination growth associated with this event in the first load step for A4 and A5.

5.3. Buckling and postbuckling behaviour

Previous analyses by Nilsson et al. (2001), indicated a very strong coupling between global plate buckling and delamination growth. Perfectly clamped boundary conditions are difficult to obtain in testing and the actual buckling load seen in a test is therefore often somewhat lower than computed ones with perfectly clamped conditions. To compensate for this boundary effect, Nilsson et al. (2001) increased the panel length in the computational model such that the computed panel buckling load matched the one seen in the

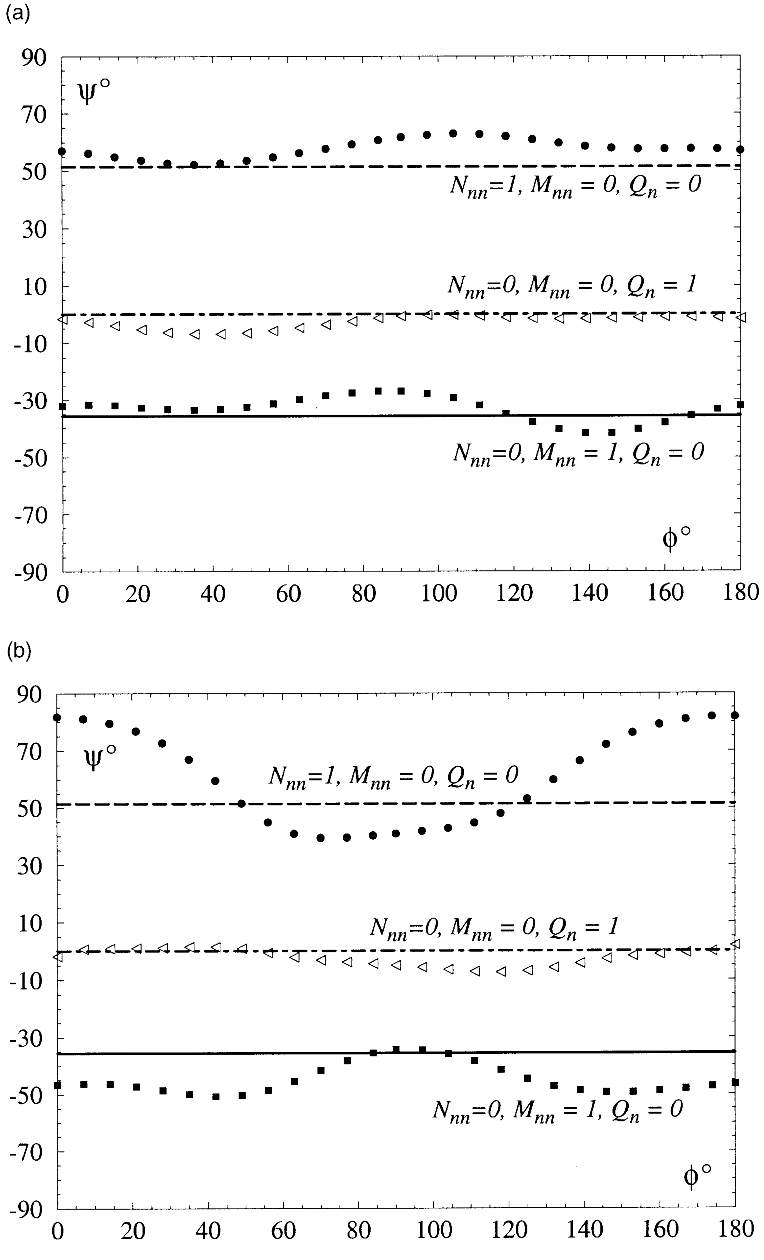

Fig. 10. Computed phase angle ψ, as function of rotation of stacking ϕ, for the in-plane unit loads as given by approximate mode separation and full generalized plane strain FE-analysis. (a) delamination at ninth interface, layup sequence: $[90+\phi/\mp45+\phi/\phi_2/\pm45+\phi/90+\phi/0+\phi/\pm45+\phi(90+\phi)_2/\mp45+\phi/\phi]_2$ and (b) delamination at fifth interface, with layup sequence: $[\phi/\pm45+\phi/(90+\phi)_2/\mp45+\phi/\phi/90+\phi/\mp45/\phi_2/\pm45+\phi/90+\phi]_2$.

experiments. In order to determine the 'apparent length' for this layup, buckling tests were performed for three undelaminated panels. The length between the steel clamps in the tests was closer to 149 than 150 mm. The registered buckling load varied between 75 and 76 kN. The computed buckling load with the free

Table 1
Plates delaminated at the 27th interface

Spec. no	P_{DB} (kN)	P_{max} (kN)	P_{growth} (kN)	δ_{growth} (mm)	Δa (mm)
1_1	15	66	65	0.37	1.6
1_2	15	67	66	0.39	2.9
1_3	12	67	66	0.40	2.6
1_4	16	66	66	0.41	1.6
1_5	8	66	66	0.44	3.0
2_1	21	68	68	0.45	6.7
2_2	21	68	68	0.45	1.5
3_1	34	69	69	0.43	6.7
3_2	29	70	70	0.43	2.9

Table 2
Plates delaminated at the nineth interface

Spec. no	P_{DB}[a] (kN)	P_{max} (kN)	P_{growth} (kN)	δ_{growth} (mm)	Δa (mm)
4_1	32	70	–	–	
4_2	32	69	68	0.91	1.0
4_3	41	69	67	0.95	2.0
4_4	40	68	67	1.01	Extended to lower clamp
5_1	67	68	–	–	–
5_2	–	70	68	1.01	1.0
5_3	60	68	68	1.05	Extended to lower clamp
6_1	–	72	72	1.16	Extended to lower clamp

[a] For these panels there is not a well-defined delamination buckling load.

length, 149 mm, equalled 79 kN. In the analysis, an increase of 1 mm of the free length corresponded to about 1 kN reduction in buckling load. The panel length (apparent length), L, used in the analysis of delaminated panels was therefore set to 154 mm.

Computed and measured reaction load, P, versus applied edge displacement, δ, are plotted in Fig. 11a and b for panels with the shallow and deep delamination respectively. We see that the computational model predicts an almost perfectly linear relationship between the edge displacement, δ, and the reaction load, P, up to the maximum load. The test results manifest a clear deviation from this linearity for the plates 5 and 2. The other test panels follow the computed results closely but with a small and consistent difference. It is difficult to distinguish from Fig. 11 if this small difference is due to a somewhat lower in-plane stiffness in the tests or to a slight deviation from linearity. The maximum load for the test panels varies within a few kN. As mentioned above, a variation of 3 mm in panel length may result in a variation of 3 kN in the computed buckling load. It therefore seems plausible that this variation for the nominally identical test panels is due to variations in free length.

Computed and measured out-of-plane deflections in the centre of the delaminated members versus the applied load, P, and edge displacement, δ, are depicted in Figs. 12 and 13 for the two delamination depths. There is generally an excellent agreement between computed and measured out-of-plane displacements versus the load, P, for both delamination depths. When out-of-plane displacement is plotted against the in-plane load, δ, there is a consistent difference at and above the global buckling load where the analysis predicts a more compliant response.

The behaviour seen for the shallow delamination is typical and has been reported earlier (e.g. Nilsson et al., 2001). The thin member deflects outwards, reaching a maximum value of about 0.9 mm at $P = 60$ kN. At this load the thicker member starts to deflect substantially in the opposite direction, pulling the thinner one along, but keeping the delamination open. The behaviour at the delamination buckling load shows

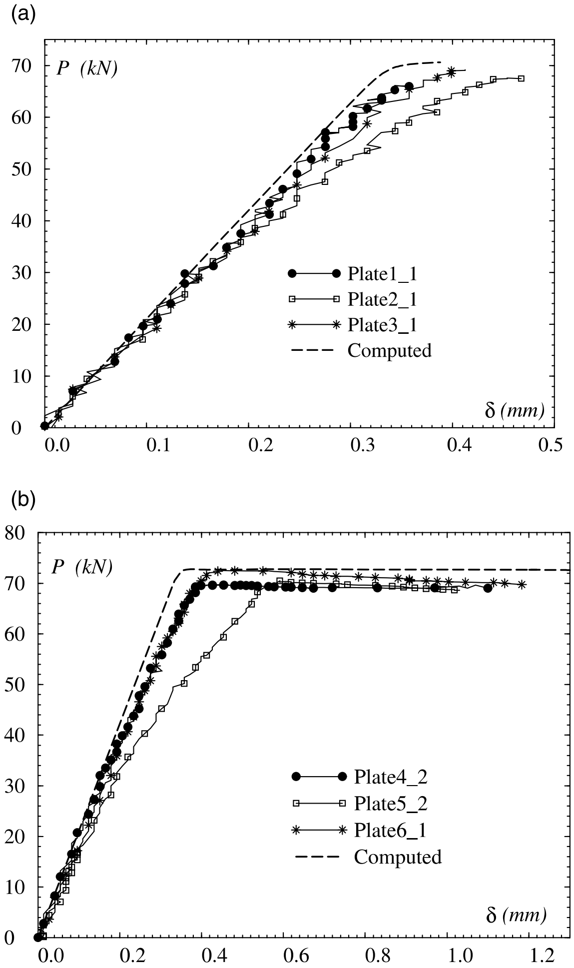

Fig. 11. Measured and computed reaction load, P, versus in-plane displacement, δ, for panels with an artificial delamination (a) shallow delamination and (b) deep delamination.

three different, but typical, behaviours that may occur in tests. Plate 1_1 has a typical imperfection of the delamination, whereas the delayed deflection seen in Plate 3_1 is due to improper separation between delaminated members. The effect is small at higher loads. If, however, the panel has a global imperfection the effect will be considerable over a wider loading range. The computed delamination buckling displacement and load were 0.112 mm and 23.1 kN. These values agree very well with test for the panel with ‘proper’ delamination buckling (0.105 mm at 21 kN).

The behaviour for the deep delamination is quite different. A small opening of the delamination was registered at the load labelled ‘delamination buckling’, P_{DB}, in Table 2. In all tests, however, the delamination closed as the maximum load was approached, followed by a drastic out-of-plane deflection. Since there is no distinct separation between the delaminated members, the concept ‘delamination buckling’ is not really adequate. In the analysis ‘buckling’, i.e. a bifurcation point was calculated at $\delta = 0.345$ mm ($P = 70.5$ kN). However, the delaminated members were in contact at the centre and remained so as the load was increased.

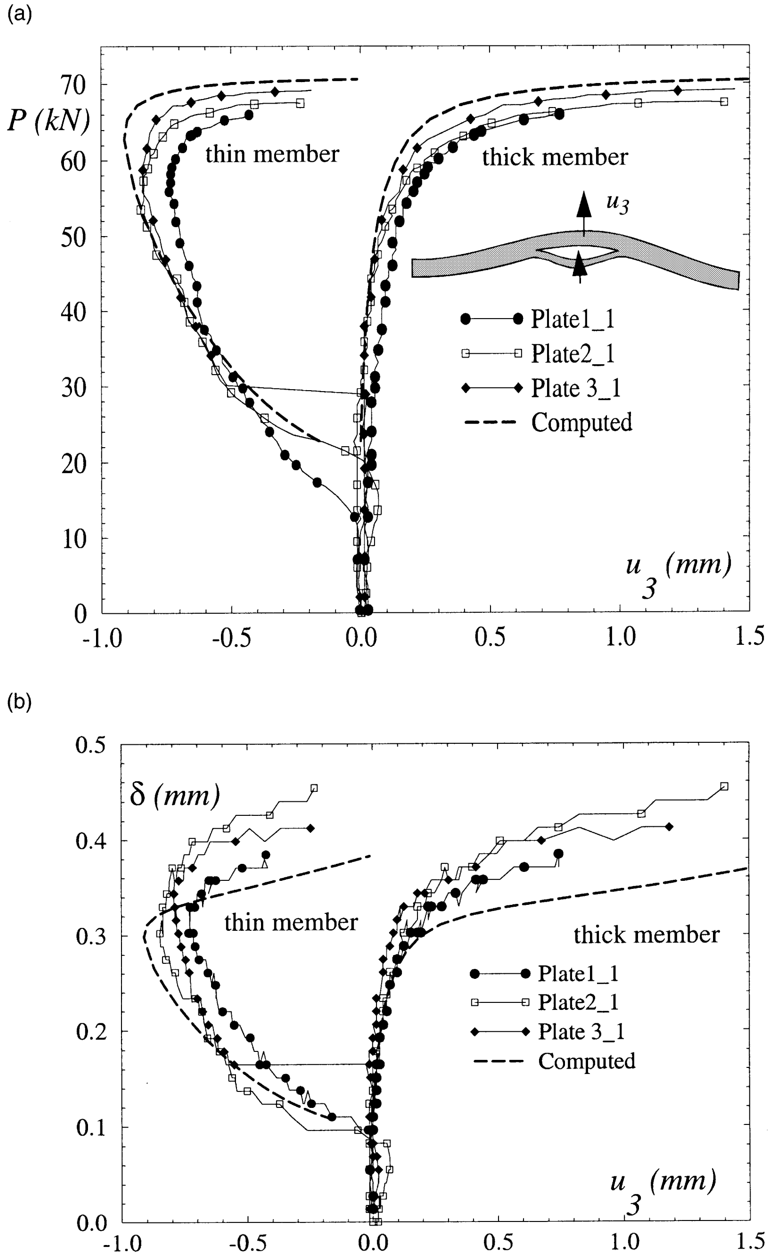

Fig. 12. Measured and computed out-of-plane deflection in the centre of the panels with shallow delamination versus (a) reaction load, P, and (b) in-plane load, δ.

In general, there is a relatively large scatter in pure Mode II fracture toughness. For this material, G_{IIc} values ranging from 640 to 1100 J/m^2 have been reported (Greenhalgh et al., 1999). The computed maximum displacement in Fig. 13, 8 mm, corresponds to a maximum energy release rate of 1100 J/m^2, but this deflection is reduced to 6 mm if the energy release rate is 640 J/m^2.

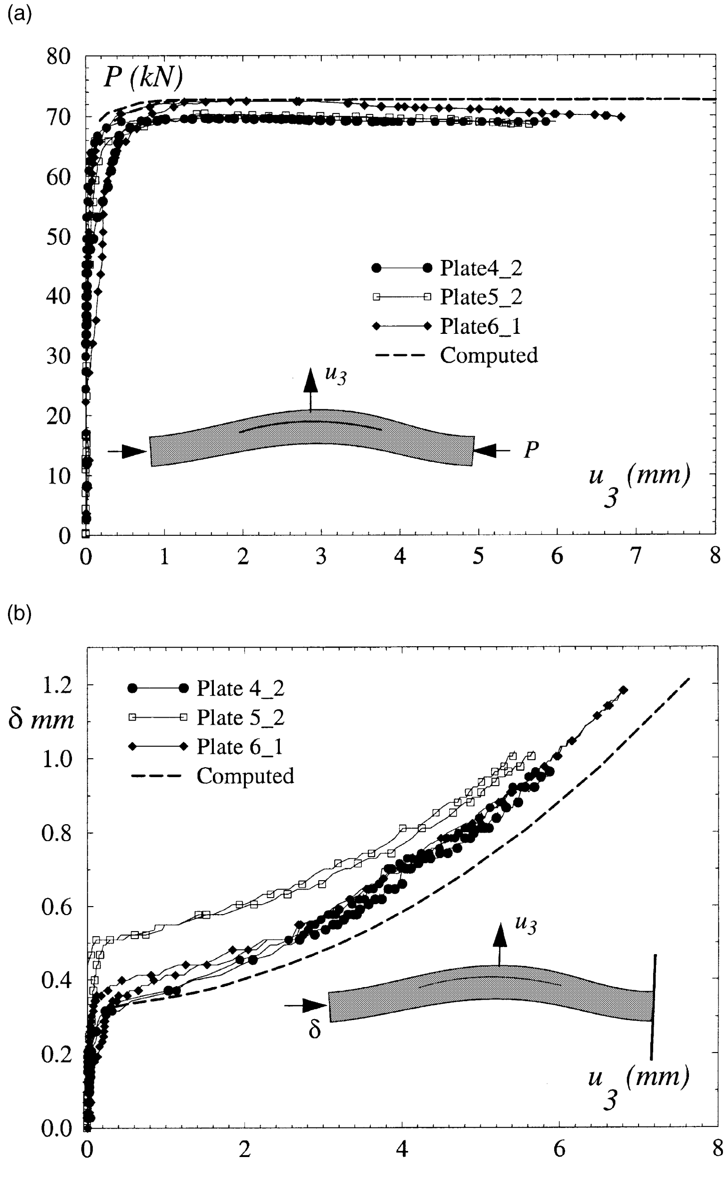

Fig. 13. Measured and computed out-of-plane deflection in centre panel with deep delamination versus (a) reaction load, P, and (b) in-plane load, δ.

5.4. Initiation of delamination growth

Onset of delamination growth can be predicted from the energy release, $G(s)$, and phase angle distributions, $\psi(s)$, together with the mixed mode fracture criterion for this material (Eq. (18)).

The computed maximum energy release rate along the front, $G_{\max}$, for the two delamination depths is plotted versus the edge displacement, δ, and reaction load, P, in Fig. 14a and b respectively. The location of $G_{\max}$ is shown in the figure inserts. For the shallow delamination, $G_{\max}$ was attained transverse to the

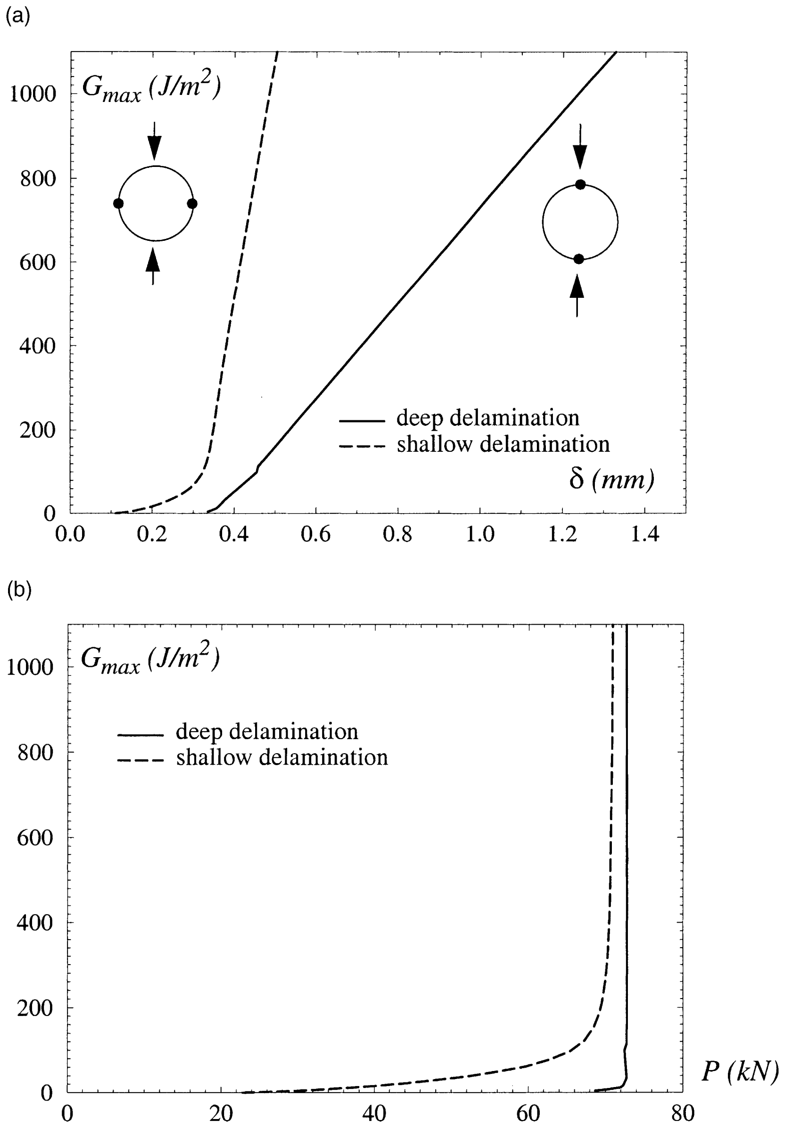

Fig. 14. Computed maximum energy release rate attained along the delamination front, $G_{\max}$, as function of (a) in-plane displacement, δ, and (b) reaction load, P. Inserts show location of $G_{\max}$.

loading direction, whereas for the deep delamination it was attained in the loading direction. It is interesting to note that in the range of critical energy release rates for this material (250–1100 J/m^2), the maximum energy release rate is almost a perfect linear function of the displacement load.

Onset of delamination growth was predicted at $\delta_{\text{growth}} = 1.23$ mm and $P_{\text{growth}} = 72.6$ kN for the deep delamination and $\delta_{\text{growth}} = 0.38$ mm and $P_{\text{growth}} = 70.5$ kN for the shallow delamination. The computed in-plane displacement corresponds very well with the test results in Tables 1 and 2. The distribution of energy release rate, G, and phase angle, ψ, along the crack front at these loads are shown in Figs. 15 and 16 respectively. The peak values for the energy release rate has shifted by 90° for the two cases and the peak is

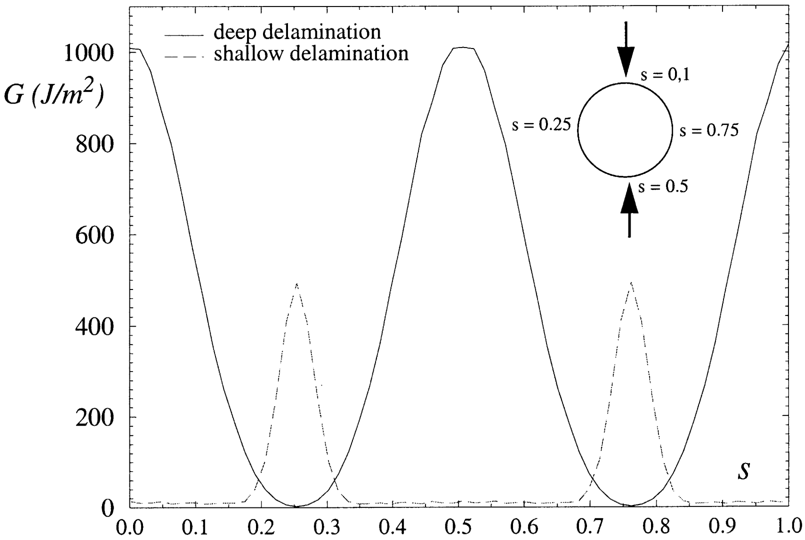

Fig. 15. Computed G-distribution at initiation of crack growth for the deep and shallow delamination respectively.

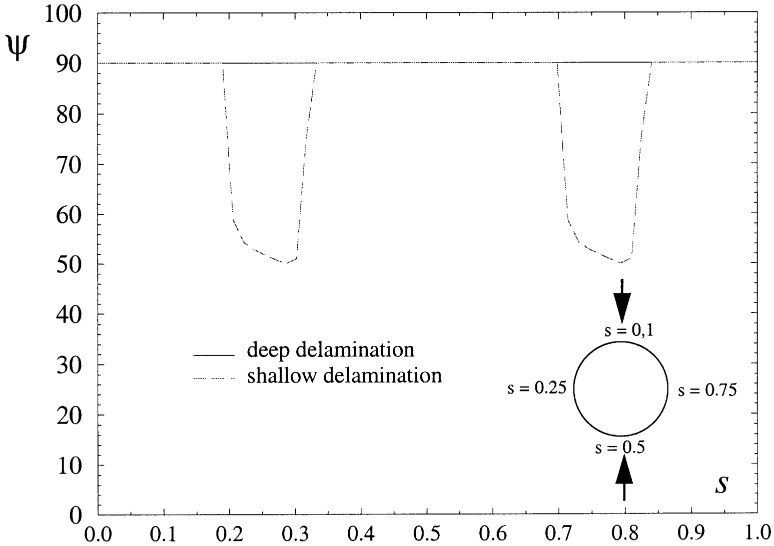

Fig. 16. Computed ψ-distribution at initiation of crack growth for the deep and shallow delamination respectively.

more narrow for the shallow delamination. The crack tip loading is Mode II along the entire front for the deep delamination, whereas for the shallow delamination, loading is mixed mode at the energy release rate peaks. It follows from the G- and ψ-distributions and the mode dependent fracture toughness, that incipient crack growth is predicted in the load direction for the deep delamination and orthogonal to the load direction for the shallow delamination; exactly the shift in growth direction seen in the tests. Ultrasonic C-scans at initiation for the two delamination depths are depicted in Fig. 17a and b. Corresponding micrographs of the delamination surfaces are shown in Fig. 18a and b. The micrograph for the shallow delamination, Fig. 18a, shows that propagation took place in the fibre/matrix interface leaving imprints in

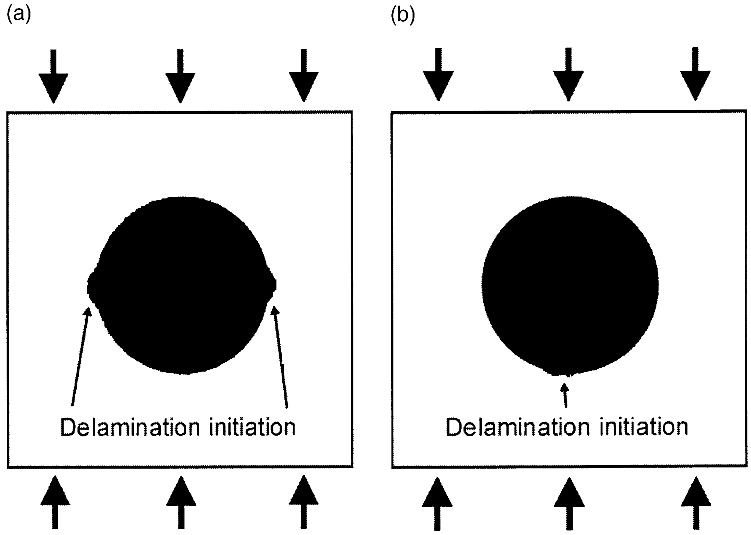

Fig. 17. Scans of initiation of delamination growth for (a) shallow delamination and (b) deep delamination.

the 27th ply. Transverse crack originating from the −45° fibre layer below are clearly seen. The transverse crack density is typical for a mixed Mode I and II loading (cf. Fig. 8e), and in line with the computed mode mixity seen in Fig. 16. The micrograph for the deep delamination (Fig. 18b) shows shear cusps typical for Mode II dominated growth illustrated in Fig. 8c. This observation together with the fact that the delaminated members were in contact support the predicted pure Mode II loading.

5.5. Delamination growth

The growth behaviour observed in the tests was quite different for the two delamination depths. For the shallow delamination, growth took place in two more or less symmetric lobes orthogonal to the load whereas for the deep delamination, growth occurred in the load direction and primarily only on one side. The most important difference, however, was that the shallow delaminations underwent stable growth, whereas the panels with a deep delamination all failed catastrophically after a few mm of growth.

Ultrasonic *C*-scans of the delaminated panels for two cases are shown in Figs. 19 and 20. The delamination growth in the specimens with a shallow delamination, initiated from the artificial delamination and propagated orthogonal to the loading direction and without change of interface. The loading was stopped as soon as there was an indication of significant acoustic emission. As we see from Table 1, delamination growth occurred in every load step and we conclude that AE-activity was always associated with delamination growth.

The delamination growth for the deep delamination had a much more complex evolution. The white arrows in Fig. 20 indicate local growth directions. The darker region represents the interface were the delamination was inserted whereas the lighter areas map delamination growth in the 10th interface (one ply deeper). The initial growth was in the loading direction and in the original interface, but at a certain stage, the delamination jumped to the next ply where also the direction of delamination growth changed. As can be seen from Table 2, there was no delamination growth after the first load step of Plates 4 and 5. This indicates that other types of damage, most likely matrix cracking, occurred prior to delamination growth. Microcracking is also indicated by Fig. 13a where we see that the load, P, reached its maximum at about $\delta = 0.6$ mm and then slightly levelled off. Such material degradation will interact with the delamination in

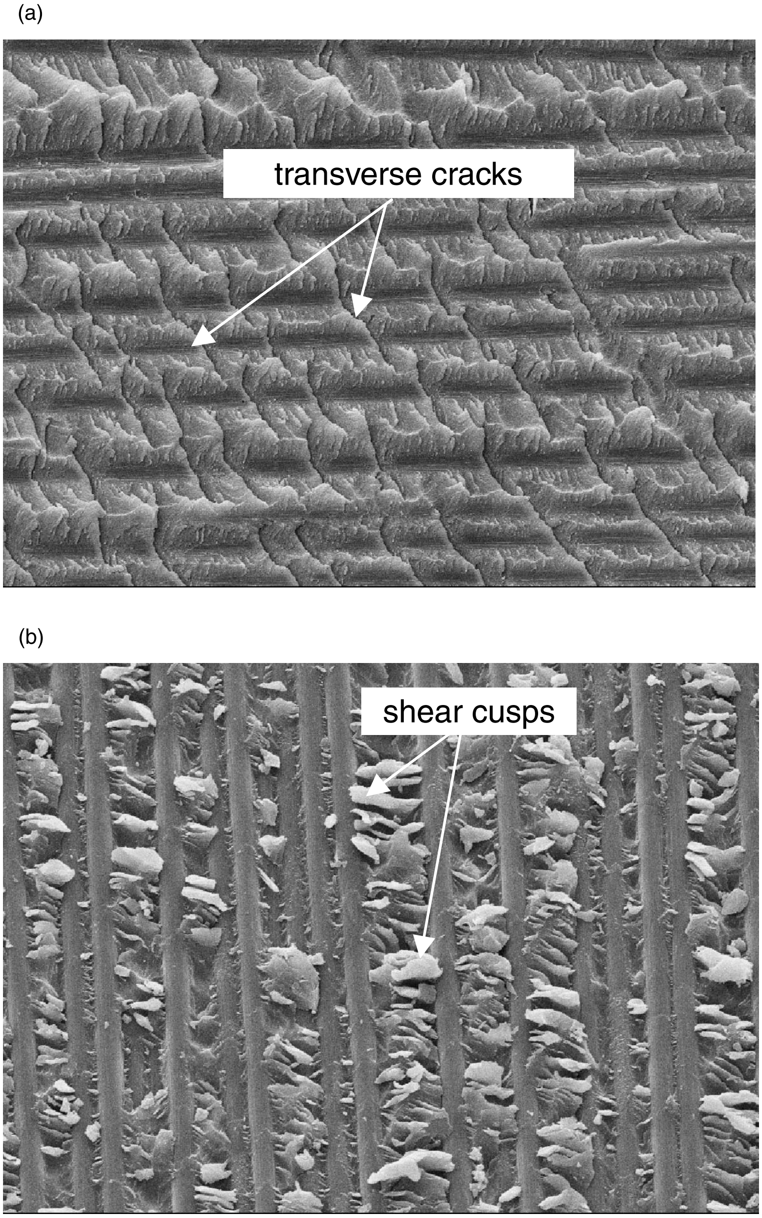

Fig. 18. Micrographs of at initiation points shown in Fig. 17 for (a) shallow delamination and (b) deep delamination.

at least two different ways. One effect is that it would lead to softening of the material. Another and perhaps more important effect is that matrix cracks close to the delamination front may trigger the delamination to migrate into a neighbouring ply interface. These effects, which are not accounted for by the model, may lead to a reduction in strength, and loss of stability and symmetry.

The predicted crack shapes at 5, 10, 15, and 23 mm delamination growth for the two delaminations depths are shown in Fig. 21 and the associated edge displacement, δ_c, required to sustain growth as function of the maximum growth at a point along the front, Δa, is shown in Fig. 22.

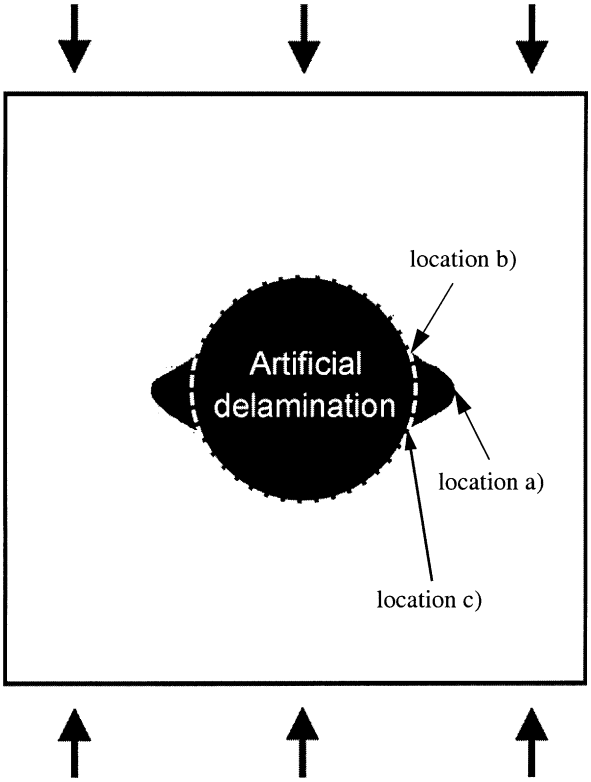

Fig. 19. *C*-scan of panel with a shallow delamination (Plate 1_5).

The predictions for the stability as well as for the evolution of the delamination front agree well with tests for the shallow delamination. However, the early loss of stability and symmetry seen in the test of the deep delamination was not captured by the model. We see, however, that instability is predicted at a much later stage when the delamination has propagated 20 mm. At this stage symmetry is also lost and the delamination growth is localized to the small region indicated in Fig. 21. The crack tip loading became also mixed mode at the location where growth occurred, (ψ about 70°).

As mentioned above, stress based failure criteria can easily be incorporated into the computational model. Even though one should be cautious about drawing conclusion from such criteria, they may give an indication of other failure mechanisms.

The computed Hashin failure criteria in the delaminated member and in the ‘remaining structure’ as function of the load for the two delamination depths are plotted in Fig. 23a and b. For the shallow delamination, the Hashin criteria predict damage only inside the delamination and by matrix compression. The situation is much more severe for the deep delamination, but in this case, it is the outside region that is critical. Matrix cracking is predicted at $\delta = 0.6$ mm, which happens to be the load when acoustic emission was registered for the plates 4_1 and 5_1 and when stiffness reduction can be seen in Fig. 13a. We also see that, according to the Hashin failure criteria, fibre compression failure is predicted prior to growth. Since most of the load is carried by the fibres, fibre failure is much more critical for the overall structural integrity. The post-mortem fractographical investigation could not identify any kink bands to support the prediction of fibre failure.

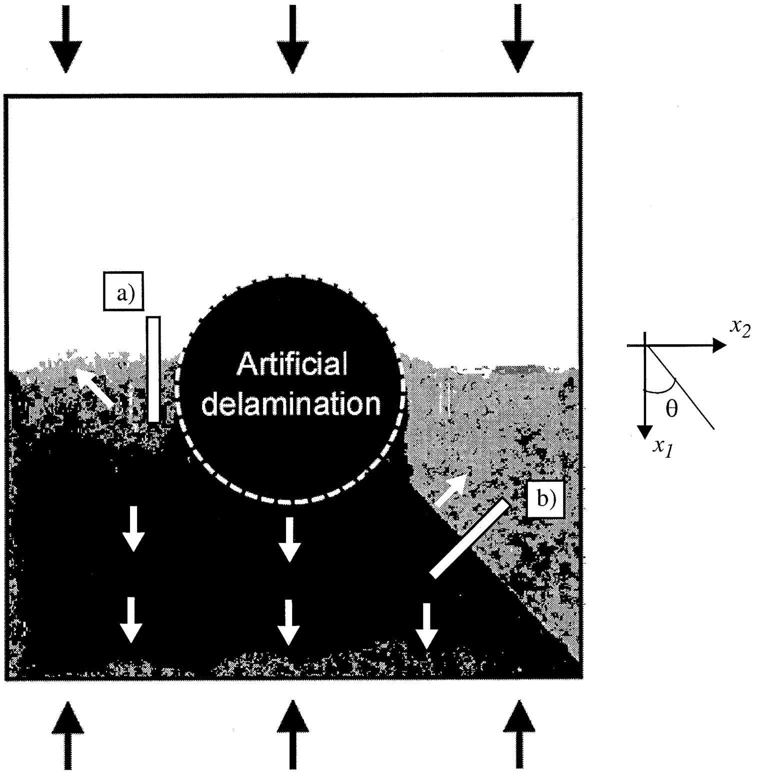

Fig. 20. *C*-scan image of a plate with deep delamination after final failure (Plate 4_4). White arrows indicate local delamination growth directions.

In order to better understand the failure mechanisms, the panels were studied in a SEM. The fracture surfaces showed that delamination growth for the shallow delamination had taken place under mixed Mode I and Mode II conditions, mainly along the 90° fibers in the 28th ply. Close to the delamination front, at location (a) in Fig. 19, there were few transverse cracks and bare 90° fibres were seen at the fracture surface of the 28th ply (see Fig. 24a). This suggests that delamination growth became more Mode I dominated as the delamination grew. Further along the artificial delamination front, at point (b) in Fig. 19, the grid pattern density increased, (cf. Fig. 18a), with a crack originating from almost every crack in the lower 45° ply, see Fig. 24b. The analysis predicted that the mode mixity was more or less retained as the delamination grew. We see from Fig. 10b that the approximate mode separation predict more Mode II loading in the growth direction than the 'reliable' one. The increased transverse cracking indicates a higher Mode II content at point (b) than at initiation. There were also signs of more pronounced shear cusps. The initial delamination growth direction at point (b) was normal to the artificial delamination, i.e. a growth direction diverging from the 45° fibres in the 27th ply and the 90° fibres in the 28th ply. Crack growth along fibres was therefore not possible. This explains the cusps and distinct grid pattern of matrix cracks. On the other side of the lobe, location (c) in Fig. 19, the growth direction more or less coincided with the 45° fibres and the delamination crack followed the fibres in the 27th ply.

The fractographical investigation of the crack surfaces for one panel with a deep delamination, Plate 4, showed that primary crack growth was in the loading direction along the 90° fibres in the ninth ply. The morphology of the fracture surface was very similar to the micrograph Fig. 18b, i.e. a large density of upright shear cusps, which suggests that loading remained pure Mode II.

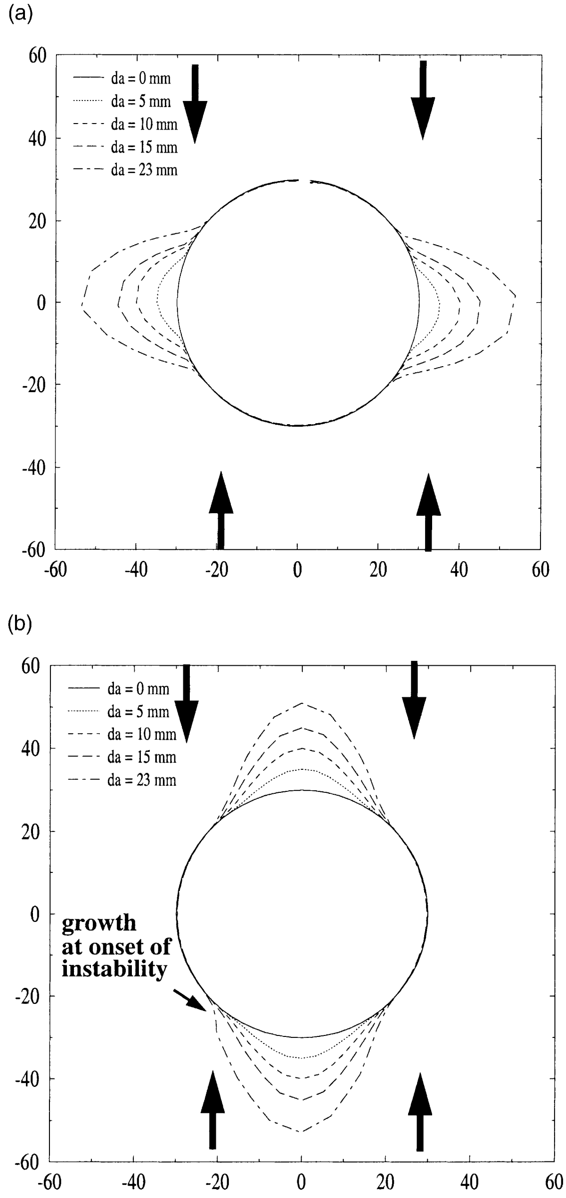

Fig. 21. Evolution of computed crack fronts for panel with (a) shallow delamination and (b) deep delamination.

As a further step in the fractographical study, segments were cut out from two different locations (see Fig. 20). Optical micrographs from polished specimens from location (a) and (b) are shown in Fig. 25. The first micrograph, taken at location (a) show a high density of transverse crack in the 90° plies as well as some transverse cracks in the +45° plies. The second micrograph, which is taken along the line where the ply jump occurred, also displays transverse cracks in the +45° plies. Transverse cracking did not occur, or at least we did not observe it, in the shallow delamination case.

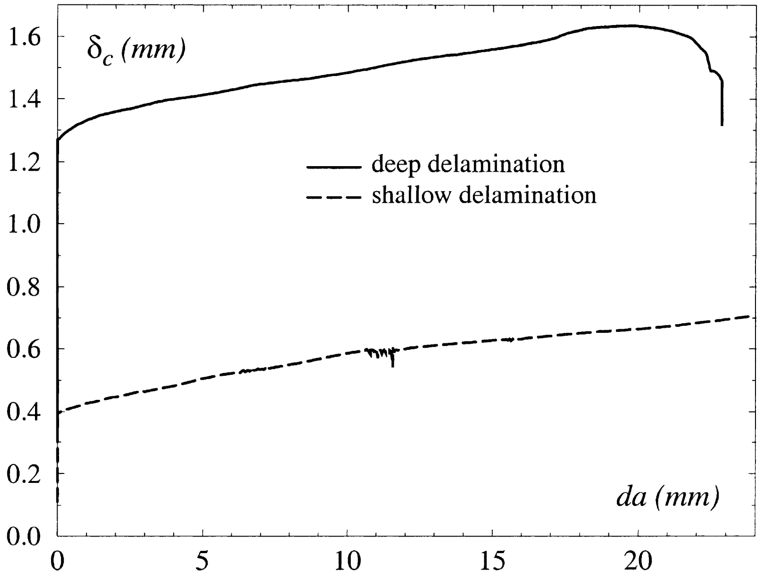

Fig. 22. Computed load required to sustain growth, δ_c, as function of maximum local delamination growth, *da* for the two delamination depths.

6. Discussion

We do not believe that the potential inaccuracy of the approximate mode separation had a significant effect in this case. That may not be the case for other tests and incorporation of the reliable mode decomposition is therefore essential. This can be done by solving the split-beam problem for the delamination depth of interest and the layup rotated at a sufficient number of angles, similar to what was done in Fig. 10 and storing the results in a database. Mode separation in the analysis is then done by appropriate interpolation of these results. A number of open issues remain with respect to appropriate growth criteria. It is well known that delaminations tend to propagate along fibres and the fracture toughness has in addition to mode mixity dependence also a fibre orientation dependence. The effect of the oscillatory stresses at bimaterial interfaces is another open issue. It should be remembered though that there is no well-defined interface for layered composite materials and as reported here delaminations often propagate just inside one of the plies. These observations suggest that there is not much to be gained by using the more consistent phase angles defined for a particular length.

The model assumes that the delamination propagates without change of interface and that no other mechanisms that reduce the structural integrity occur. The fractographical investigation, as well as registered acoustic emission activity prior to delamination growth, clearly showed that other damage, in particular transverse cracking, was present in the tests. We believe that the discrepancy between tests and predictions was due to this additional damage. Such additional damage will always be present in the case of impact damage. If we want to predict failure in more general situations all relevant failure mechanisms and their interaction need to be taken into account. This may become an overwhelming task unless certain simplifying assumptions are made. In our opinion, the most natural extension to include these effects would be to retain the explicit modelling of delaminations but account for other failure mechanisms by simple local stress based criteria and modified constitutive behaviour. Such a model extension requires, however, that at least three new problems must be handled.

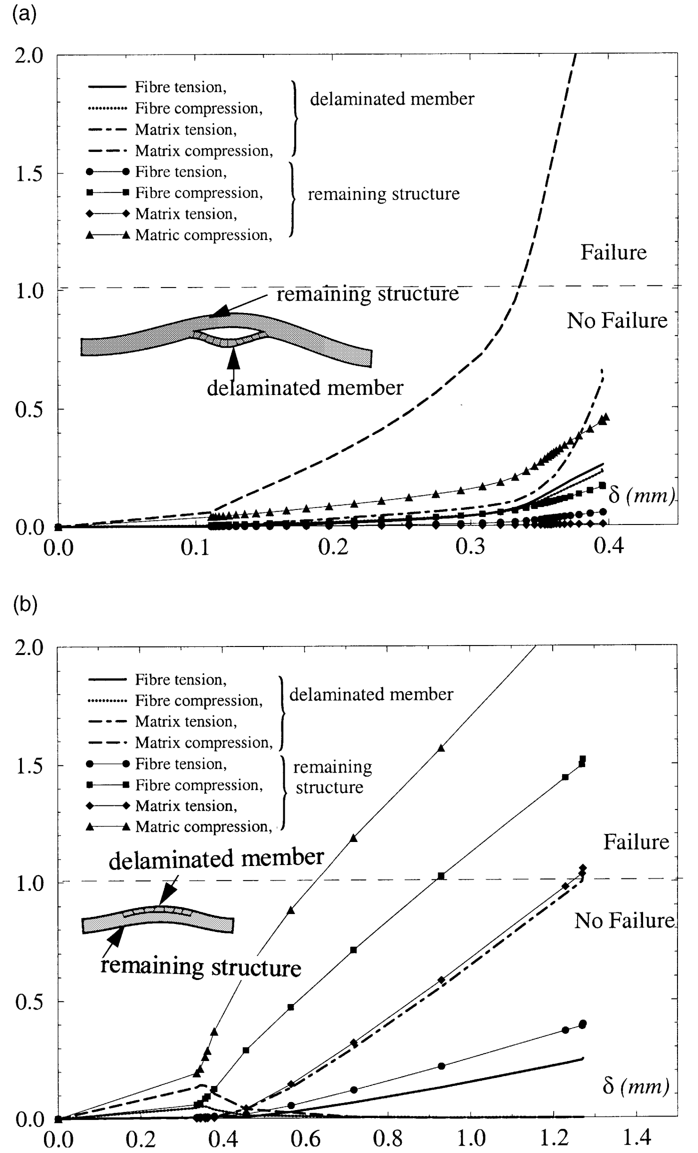

Fig. 23. Computed normalized Hashin failure factor versus applied in-plane displacement in delaminated member and remaining panels at onset of delamination growth for the two delamination depths (a) shallow delamination and (b) deep delamination.

Firstly, we need a measure for onset of damage. The Hashin failure criteria could be such candidates for matrix cracking and fibre failure. Ply-jumping depends on the fracture toughness of the interface and the materials on either side of the delamination. It has been shown for isotropic bi-materials by He and Hutchinson (1989) and He et al. (1991) that kinking can be predicted from the different fracture toughnesses, the mode-mixity and T-stresses. A methodology in this spirit could be adopted in our methodology.

Secondly, the effect of the damage, whether it is as a stiffness reduction or as a catalyst for other events, e.g. ply jumping should be modelled. This may become a formidable problem since the degradation will be different in compression and tension as well heterogeneous. There are a large number of papers in the

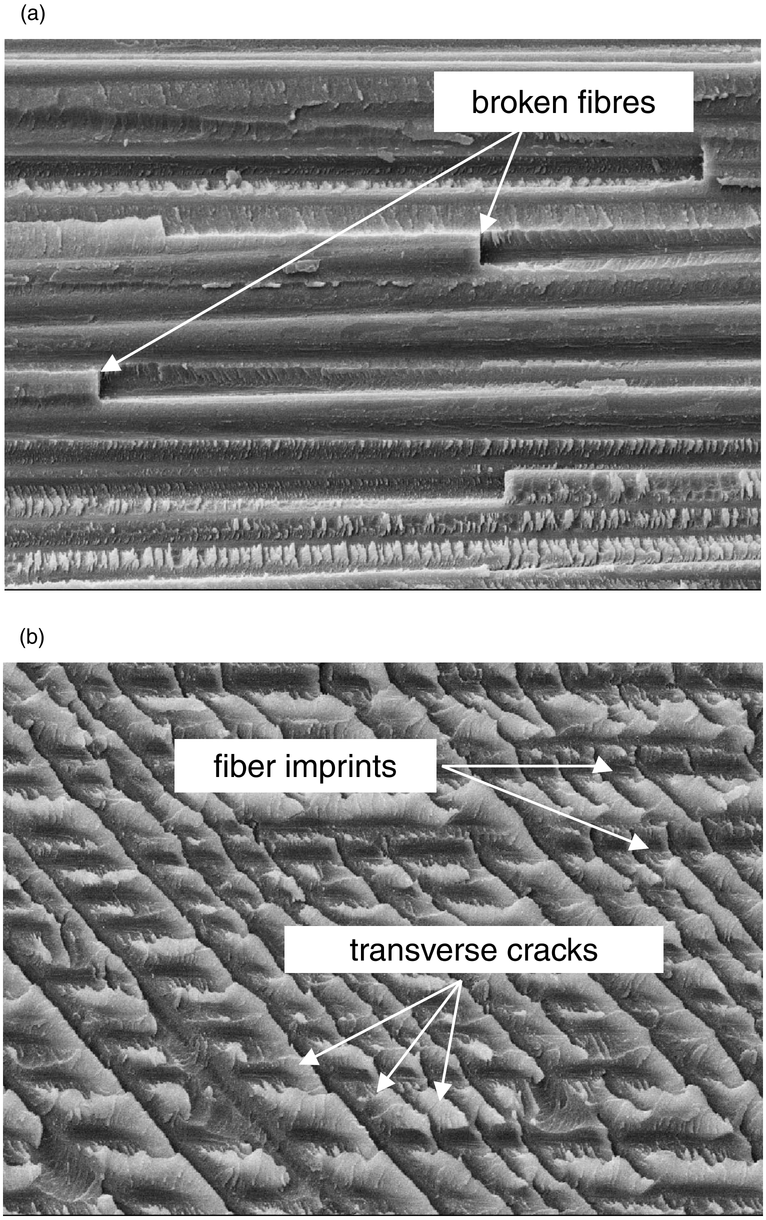

Fig. 24. Micrographs of shallow delamination at the two locations (a) and (b) given in Fig. 19.

literature about how to account for such effects e.g. shear-lag models (Smith and Wood, 1990), variational model (Hashin, 1985; Varna and Berglund, 1994), continuum damage models, (Talreja, 1990); exact analytical expressions for certain idealized cases (Gudmundson and Zang, 1993). The natural way would be to see if any of these could do a good job.

Thirdly, the change in constitutive properties may lead to very intricate structural problems such as loss in stability due to softening and the inherently three-dimensional effects that arise in interaction between

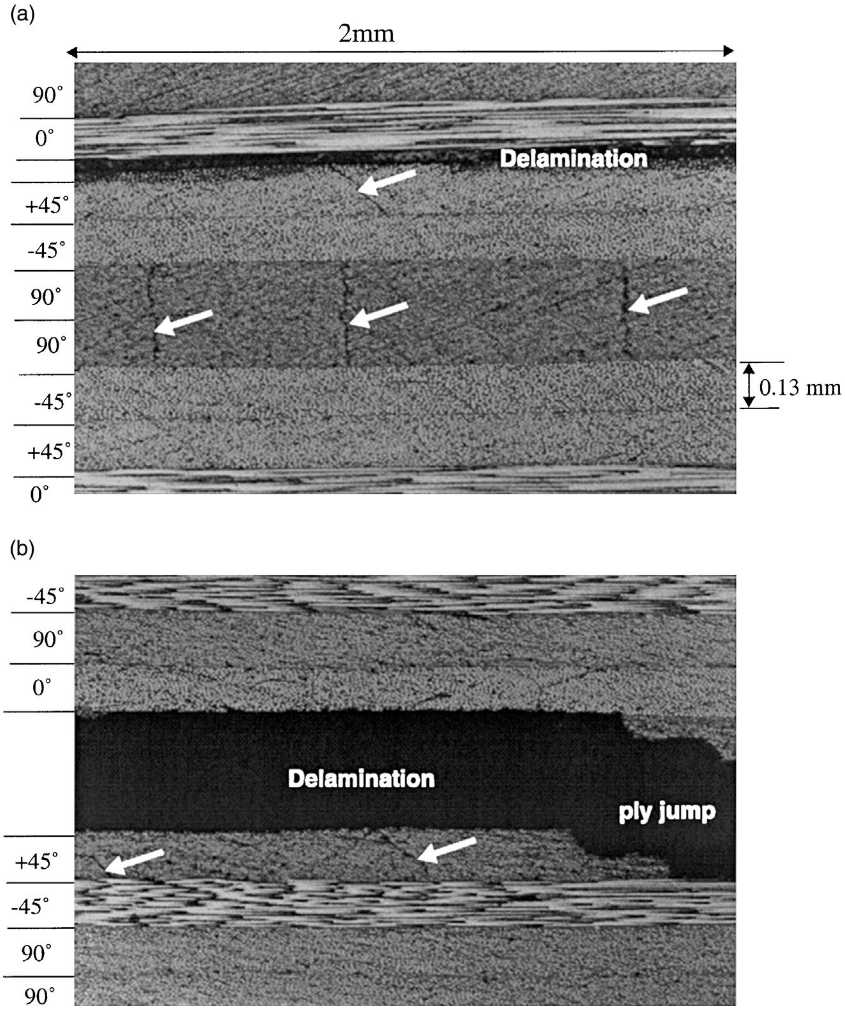

Fig. 25. Optical micrographs of polished segments of panel 5 taken from the two locations (a) and (b) given in Fig. 20. White arrows indicate transverse cracks.

delamination and matrix cracks and locally at a ply-jump. These may require full three-dimensional analyses.

7. Conclusions

A combined theoretical/numerical and experimental investigation on the transition of the delamination growth behaviour for slender composite panels loaded in compression has been presented. The work was initiated by a computational parameter study where we sought for particular geometry and material combinations where embedded delaminations may propagate in the load direction as opposed to the well documented growth in the transverse direction. Such a transition was predicted to occur as the location of a delamination was changed from the 27th interface (shallow delamination) to the nineth (deep delamination) of a panel with 32 plies in quasi-isotropic layup. Tests were then performed and the predicted transition was observed. The change of delamination depth did not only change the direction of growth, but growth also changed from mixed mode to pure Mode II and symmetry of delamination growth was lost. More importantly though, growth switched from being stable to unstable. Test and predictions agreed very well for the shallow delamination. The change in growth direction for the deep delamination was also captured by the model as well as the change to pure Mode II crack growth, while the loss of symmetry and stability were predicted at a much later stage. This discrepancy suggests that there could be other mechanisms, not taken into account in the modelling, that interact with the delamination. Further research is needed to understand such interaction better.

Contemporary design of composite aircraft structures does not allow for damage growth. Development of models of the type described above may, however, result in aircraft designs that allow for controlled damage growth.

Acknowledgements

This work has been funded by the Swedish Materiel Administration (FMV) and the European Commission under contract no. BRPR-CT98-0611, which is gratefully acknowledged.

References

Andersson, B., Babuska, I., Falk, U., 1990. Accurate and reliable determination of edge and vertex stress intensity factors in three-dimensional elastomechanics. ICAS-90-4.9.2, Proceedings of 17th congress of the International Council of the Aeronautical Sciences, Stockholm, Sweden, pp. 1730–1746.

Andersson, B., 1993. Calculation of fracture mechanics parameters from measured surface displacements in composite specimens. Proceedings from Sixth Nordic Seminar on Computational Mechanics, 18–19 October, University of Linköping, pp. 181–184.

Asp, L.E., Nilsson, S., Singh, S., 1999. An experimental investigation of the influence of delamination growth on the residual strength of impacted laminates, FFA TN 1998-52, The Aeronautical Research Institute of Sweden. Proc. Euromech Colloqium 400, London, UK, in press.

Asp, L.E., Sjögren, A., Greenhalgh, E.S., 2001. Delamination growth in a carbon/epoxy composite under fatigue loading. J. Compos. Technol. Res. 23, 55–68.

Choi, N.S., Kinloch, A.J., Williams, J.G., 1999. Delamination fracture of multidirectional carbon-fiber/epoxy composites under mode I, mode II and mixed-mode I/II loading. J. Compos. Mater. 33, 73–101.

Gudmundson, P., Zang, W., 1993. A universal model for the thermoelastic properties of micro cracked composite laminates. Int. J. Solids Struct. 30, 3211–3231.

Greenhalgh, E., Singh, S., Nilsson, K.-F., 2000. Mechanisms and modelling of delamination growth and failure of carbon-fibre reinforced skin-stringer panels, ASTM STP 1383 Composite Structures: Theory and Practice. In: Grant, P., Rousseau, C.Q. (Eds.), American Society for Testing and Materials, West Conshohocken, P.A. pp. 1–33.

Greenhalgh, E.S., Asp, L.E., Singh, S., 1999. Delamination resistance, failure criteria and fracture morphology of 0°/0°, 0°/5° and 0°/90° ply interfaces. CFRP, Proceedings of the 5th International Conference on Deformation and Fracture of Composites, London, UK.

Hahn, H.T., Johannesson, T., 1983. A correlation between fracture energy and fracture morphology in mixed-mode fracture of composites. Proceedings of the 4th International Conference on the Mechanical Behaviour of Materials, Stockholm, Sweden, pp. 431–438.

Hashin, Z., 1980. Failure criteria for unidirectional fiber composites. J. Appl. Mech. 47, 329–339.

Hashin, Z., 1985. Analysis of cracked laminates: a variational approach. Mech. Mater. 4, 121–136.

He, M.-Y., Hutchinson, J.W., 1989. Kinking of a crack out of an interface. J. Appl. Mech 56, 270–278.

He, M.-Y., Bartlett, A., Evans, A.G., Hutchinson, J.W., 1991. Kinking of a crack out of an interface: role of in-plane stress. J. Am. Ceram. Soc. 74, 767–771.

Hutchinson, J.W., Suo, Z., 1992. Mixed mode cracking in layered materials. Adv. Appl. Mech. 28, 63–191.

Juntti, M., Asp, L.E., Olsson, R., 1999. Assessment of evaluation methods for the mixed-mode bending test. J. Compos. Technol. Res. 21, 37–48.

Levin, K., Jarlås, R., 1997. Vulnerability of embedded EFPI-sensors to low-energy impact. Smart Mater. Struct. 6, 369–382.

Lekhnitskii, S.G., 1963. Theory of elasticity of an anisotropic body, Holden-Day, San Francisco, USA.

Nilsson, K.-F., Storåkers, B., 1992. On the interface crack growth in composite plates. J. Appl. Mech. 59, 530–538.

Nilsson, K.-F., Thesken, J.C., Sindelar, P., Giannakopoulos, A., Storåkers, B., 1993. A theoretical and experimental investigation of buckling induced delamination growth. J. Mech. Phys. Solids 41, 749–782.

Nilsson, K.-F., Asp, L.E., Alpman, J.E., Nystedt, L., 2001. Delamination buckling and growth for delaminations at different depths in a slender composite panel. Int. J. Solids Struct. 38, 3039–3071.

Purslow, D., 1986. Matrix fractography of fibre-reinforced epoxy composites. Composites 17, 289–303.

Rice, J.R., 1988. Elastic fracture mechanics concepts for interfacial cracks. J. Appl. Mech. 55, 98–103.

Sheinman, I., Kardomateas, G.A., 1997. Energy release rate and stress intensity factors for delaminated composite laminates. Int. J. Solids Struct. 34, 451–459.

Singh, S., Greenhalgh, E., 1998. Micromechanisms of interlaminar fracture in carbon fibre reinforced plastics at multidirectional ply interfaces under static and cyclic loading. Plast. Rubb. Compos. Proc. Appl. 27, 220–226.

Smith, P.A., Wood, J.R., 1990. Poisson's ratio as damage parameter in the static tensile loading of simple cross-ply laminates. J. Comp. Tech. Res. 38, 85–93.

Suo, Z., Hutchinson, J.W., 1990. Interface crack between two elastic layers. Int. J. Fracture 43, 1–18.

Talreja, R., 1990. Internal variable damage mechanics of composite materials. In: Boehler, J.P. (Ed.), Yielding, Damage and Fracture of Anisotropic Solids. Mechanical Engineering Publications, London, pp. 509–533.

Varna, J., Berglund, L.A., 1994. Thermo-elastic properties of composite laminates with transverse cracks. J. Comp. Tech. Res. 16, 77–87.

Wang, S.S., Choi, I., 1982. Boundary-layer effects in Composite laminates: Part 1 – Free-edge stress singularities, Part 2 – Free edge stress solutions and basic characteristics. J. Appl. Mech 49, 541–560.

Whitcomb, J.D., 1986. Parametric analytical study of instability-related delamination growth. Compos. Sci. Technol. 25, 19–48.

Whitcomb, J.D., 1989. Three-dimensional analysis of a post-buckled embedded delamination. J. Compos. Mater. 23, 862–889.